ARTICLES
https://doi.org/10.1038/s41593-020-0647-1

nature neuroscience

Cross-hemispheric gamma synchrony between prefrontal parvalbumin interneurons supports behavioral adaptation during rule shift learning

Kathleen K. A. Cho[1,2,3], Thomas J. Davidson[2,4,5], Guy Bouvier[4,5], Jesse D. Marshall[6], Mark J. Schnitzer[7,8] and Vikaas S. Sohal[1,2,3]✉

Organisms must learn new strategies to adapt to changing environments. Activity in different neurons often exhibits synchronization that can dynamically enhance their communication and might create flexible brain states that facilitate changes in behavior. We studied the role of gamma-frequency (~40 Hz) synchrony between prefrontal parvalbumin (PV) interneurons in mice learning multiple new cue–reward associations. Voltage indicators revealed cell-type-specific increases of cross-hemispheric gamma synchrony between PV interneurons when mice received feedback that previously learned associations were no longer valid. Disrupting this synchronization by delivering out-of-phase optogenetic stimulation caused mice to perseverate on outdated associations, an effect not reproduced by in-phase stimulation or out-of-phase stimulation at other frequencies. Gamma synchrony was specifically required when new associations used familiar cues that were previously irrelevant to behavioral outcomes, not when associations involved new cues or for reversing previously learned associations. Thus, gamma synchrony is indispensable for reappraising the behavioral salience of external cues.

Adapting to a changing environment requires detecting when behavioral strategies become outdated and then suppressing them and learning new ones. Deficits in this ability are hallmarks of prefrontal dysfunction in schizophrenia, classically measured by the Wisconsin Card Sorting Task[1,2]. Many natural behaviors also involve rapidly learning new strategies that use external cues that were previously unimportant. Mechanisms underlying this kind of adaptation remain unknown. Synchrony between activity in different neurons might regulate how those neurons interact with each other and their downstream targets[3–13]. Thus, by transiently enhancing interactions between specific neurons, synchrony could generate dynamic brain states that facilitate behavioral adaptation. Synchronized gamma-frequency (~30–80 Hz) activity occurs in the medial prefrontal cortex (mPFC) when rodents change behavior[14–16]. Interneurons, particularly those expressing PV, generate synchronized gamma-frequency activity. However, it remains deeply controversial whether gamma synchrony between activity in different regions contributes to behavior or simply reflects increased PV interneuron recruitment[17,18].

To address this, we studied a task involving the type of behavioral adaptation outlined above[14,15,19–21]. In each trial, mice chose between two bowls to find hidden food rewards (Fig. 1a,c). Each bowl contained different odor and texture cues. Mice first formed an initial association between one cue and reward and then learned a 'rule shift' from odor to texture (or vice versa). By contrast, during a 'rule reversal', the type of rule (odor or texture) did not change, but the previously unrewarded cue then became rewarded (Fig. 1b). Unlike tasks requiring well-trained mice to switch between previously learned behaviors, in this task, mice formed new associations using familiar cues that were previously either irrelevant (rule shift) or predictive (rule reversal) with respect to behavioral outcomes.

Several observations indicate that rule shifts, but not rule reversals, depend on interneuron-generated rhythmic mPFC activity. mPFC lesions disrupt rule shifts but not rule reversals[19]. Inhibiting prefrontal GABAergic interneurons similarly disrupts rule shifts but not initial associations or rule reversals[14], and mutant mice with abnormal PV interneurons and deficient task-evoked mPFC gamma power have the same pattern of impairments[14]. In these mutant mice, stimulating prefrontal interneurons at gamma frequencies (40–60 Hz) normalizes learning during rule shifts[14]. Thus, synchronized gamma-frequency mPFC activity can improve pathological behavior, although its role in normal behavior remains unclear. In fact, gamma-frequency stimulation of prefrontal interneurons improves sensory detection, attention and social behavior[22–24]. However, none of these studies directly addressed two fundamental questions. First, do these behavioral effects require synchronization across brain regions, or is enhancing rhythmic inhibition within local circuits sufficient? Second, even if artificially increasing synchrony improves behavior, is naturally occurring synchrony necessary for normal behavior?

In this study, we explored how cross-hemispheric gamma synchrony between prefrontal PV interneurons contributes to learning during rule shifts. Gamma-frequency synchrony between PV interneurons in the left and right mPFC increased during rule shifts but not during initial associations or rule reversals. Delivering weak gamma-frequency optogenetic stimulation out-of-phase between the left and right mPFC disrupted rule shifts, whereas in-phase stimulation had no effect. This disambiguates the role

[1]Department of Psychiatry, University of California, San Francisco, San Francisco, CA, USA. [2]Kavli Institute for Fundamental Neuroscience, University of California, San Francisco, San Francisco, CA, USA. [3]Weill Institute for Neuroscience, University of California, San Francisco, San Francisco, CA, USA. [4]Department of Physiology, University of California, San Francisco, San Francisco, CA, USA. [5]Howard Hughes Medical Institute, San Francisco, CA, USA. [6]Department of Organismic & Evolutionary Biology, Harvard University, Cambridge, MA, USA. [7]Departments of Biology and Applied Physics, Stanford University, Stanford, CA, USA. [8]Howard Hughes Medical Institute, Stanford, CA, USA. ✉e-mail: vikaas.sohal@ucsf.edu

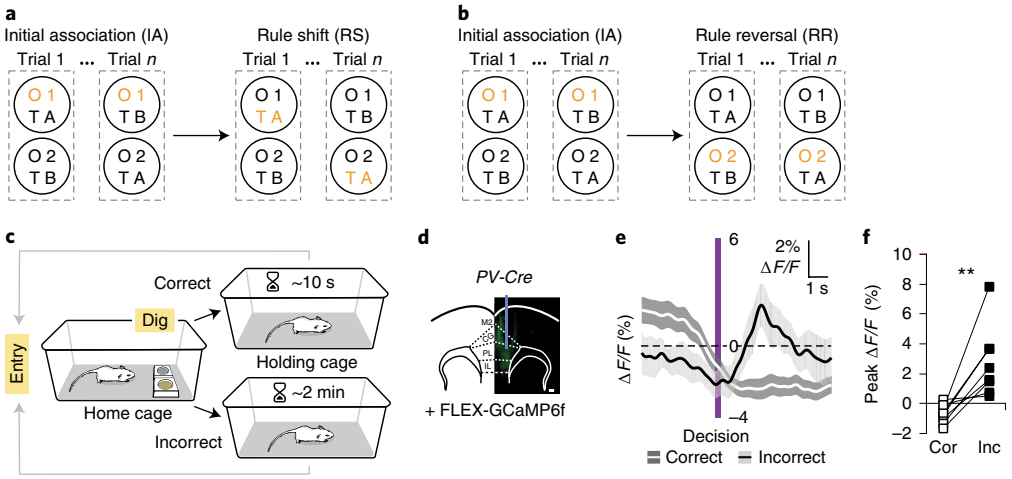

Fig. 1 | Prefrontal PV interneurons are recruited after errors during rule shifts. a, Rule shift task schematic. On each trial, a mouse chooses one of two bowls, each scented with a different odor (O1 or O2) and filled with a different textured digging medium (TA or TB), to find a food reward. Mice first learn an initial association (IA) between one of these cues (for example, odor O1) and food reward (the cue associated with reward is indicated in orange). Once mice reach the learning criterion (8 of 10 consecutive trials correct), this association undergoes an extra-dimensional rule shift (RS; for example, from O1 to TA). **b**, Rule reversal task schematic. Mice learn an IA between one cue (for example, odor O1) and food reward (the rewarded cue is indicated in orange). Once mice reach the learning criterion, this association undergoes an intra-dimensional rule reversal (RR) (for example, from O1 to O2). **c**, Trial timeline. A mouse begins each trial by entering the home cage and then makes a decision, indicated by digging in one bowl. If the mouse is correct, the food reward is consumed. The mouse is then transferred to the holding cage until the next trial. The intertrial interval (ITI) is longer after incorrect choices. **d**, Representative image showing mPFC FLEX-GCaMP6f expression in a *PV-Cre* mouse (scale bar, 100 µm). **e**, Averaged PV interneuron photometry signal ($\Delta F/F$), aligned to the time of dig, which indicates a decision, for correct (white line) versus incorrect trials (black line; $n = 8$ mice). **f**, Peak $\Delta F/F$ during the 4 s after the decision. Signals are significantly higher on incorrect than correct trials ($n = 8$ mice; two-tailed paired *t*-test, $t_{(7)} = 3.93$, $^{**}P = 0.006$). Data are shown as means (**e**); shading denotes s.e.m.

of cross-hemispheric synchrony from that of rhythmic inhibition within a local circuit. Furthermore, perturbing cross-hemispheric synchrony did not affect initial associations or rule reversals. Thus, there was a 1:1 correspondence between whether a type of learning normally elicits increased gamma synchrony and whether it was disrupted when that synchrony is perturbed.

Results

PV interneurons are recruited after rule shift errors. We used bulk calcium imaging[25,26] (fiber photometry) to explore how PV interneurons are normally recruited during rule shifts (Fig. 1d–f and Extended Data Fig. 1). We injected AAV1-Syn-FLEX-GCaMP6f[27] into the mPFC of *PV-Cre* mice and implanted an optical fiber to measure fluorescence (Fig. 1d). We examined activity time locked to trial start, decisions (indicated by digging in one bowl), trial end (cessation of digging) and intertrial intervals (ITIs) (Fig. 1c). Supplementary Videos 1–4 show task mechanics and time-locked photometry traces. On error trials, PV interneuron activity increased after decisions—that is, when animals failed to receive rewards that would have been expected based on the previously learned association (Fig. 1e,f). PV activity did not increase after correct decisions (Fig. 1e,f). Because rule shifts were uncued, the absence of expected rewards signaled that previously learned associations were no longer valid.

Cross-hemispheric gamma synchrony between PV interneurons increases after rule shift errors. We examined whether this PV activity at critical behavioral timepoints was associated with gamma-frequency synchronization across sites using trans-membrane electrical measurements performed optically (TEMPO). TEMPO uses bulk fluorescence from the voltage indicator Ace2N-4AA-mNeon ('Ace–mNeon') to monitor specific cell types[28]. We injected AAV into the mPFC bilaterally to drive Cre-dependent Ace–mNeon expression in *PV-Cre* Ai14 mice and implanted optical fibers to measure Ace–mNeon and tdTomato fluorescence from PV interneurons in the left and right mPFC (Fig. 2a,b). Some mice were additionally injected with AAV1-Synapsin-tdTomato. tdTomato provides non-voltage-dependent reference signals. We measured signals from both prefrontal cortices (Fig. 2c) while mice learned an initial association and rule shift (Fig. 2d).

Fluorescence from genetically encoded voltage indicators is strongly contaminated by hemodynamic artifacts[28,29] such that non-neuronal artifacts dominate conventional spectral analyses of these signals (power or coherence). Previous studies addressed this using unsupervised methods to separate signal from noise in single-site recordings[28,29]. However, they did not resolve gamma-frequency signals in freely behaving mice. We overcame this barrier by leveraging dual-site recordings. To quantify zero-phase-lag cross-hemispheric synchronization, we filtered all signals around a frequency of interest and then predicted the right Ace–mNeon signal using a linear model based on the left Ace–mNeon signal, left tdTomato signal and right tdTomato signal (Fig. 2e). At every point in time, we compared this model's performance to predictions from 100 models that used the actual tdTomato signals but time-shifted versions of the left Ace–mNeon signal. The tdTomato signals captured shared sources of noise (hemodynamic signals, movement artifacts and fiber bending), and the shuffled left Ace–mNeon signal matched the degrees of freedom. Thus, the degree to which the model based on actual signals outperforms those based on shuffled signals should reflect the amount of information the left Ace–mNeon signal carries about the right Ace–mNeon signal—that is, the (zero-phase-lag) cross-hemispheric synchronization between prefrontal PV interneurons. This metric measures synchrony within a band centered around a frequency of interest, for example 30–50 Hz, which reflects synchrony at ~40 Hz. Using this method, we analyzed the first five rule shift trials (Fig. 2f–i).

(We hypothesized that these trials are crucial for learning and hence most likely to exhibit learning-related signals). Cross-hemispheric PV interneuron synchronization at 30–50 Hz was significantly higher after errors than at baseline or after correct decisions (Fig. 2f–i). Notably, error-related synchrony was frequency specific. For both lower (15–25 Hz) and higher (50–70 Hz) frequency bands, cross-hemispheric PV interneuron synchronization was similar at baseline, after correct decisions and after errors.

Synchronization at arbitrary phase lags can be expressed as the sum of in-phase and 90-degree out-of-phase components. Therefore, to explore potential synchrony at non-zero phase lags, we measured synchronization using left mPFC PV interneuron Ace–mNeon signals that were phase-shifted 90 degrees (Extended Data Fig. 2). In this case, there were no differences in 30–50-Hz synchronization at baseline versus after correct or incorrect decisions (Extended Data Fig. 2); it is specifically the zero-phase-lag component of gamma-frequency synchronization that increases after rule shift errors. We also measured voltage dynamics from somatostatin (Sst) interneurons using *Sst-Cre* mice (Fig. 2j–m and Extended Data Fig. 3a–d). Cross-hemispheric synchrony between prefrontal Sst interneurons did not increase after errors, even though, similarly to PV interneurons, Sst interneuron photometry signals increased after rule shift errors (Extended Data Fig. 3e–i). Thus, the synchronization we found was specific for trial outcome, frequency, phase lag and cell type. These are controls for nonspecific artifacts related to movement, respiration and hemodynamics.

Increased gamma synchrony also occurs in LFP recordings. To validate that TEMPO tracks aspects of network activity that can also be measured in other ways, we simultaneously recorded TEMPO signals and local field potentials (LFPs) from the left and right mPFC during rule shifts. Zero-phase-lag synchronization computed from left versus right mPFC LFPs reproduced our key TEMPO finding: ~40-Hz cross-hemispheric synchrony increases for errors during rule shifts, compared to correct trials (Fig. 2n–p). Notably, in LFP recordings, lower-frequency synchrony also increased (Fig. 2p), possibly reflecting the fact that TEMPO is cell type specific, whereas LFP recording is not. Thus, within PV interneurons, increases in ~40-Hz synchrony might be most prominent, whereas other cell types might generate LFP synchrony at lower frequencies.

Increased gamma synchrony is specific for rule shifts. Next, we examined whether increased gamma synchrony is specific for rule shifts or more generically reflects error detection or reinforcement. First, the increases in PV interneuron photometry signals that follow rule shift errors did not occur after initial association errors (Fig. 3a–d). Second, TEMPO showed no differences between cross-hemispheric PV interneuron gamma synchrony on correct versus incorrect trials during initial associations (Fig. 3g) or rule reversals (Fig. 3h). Thus, 30–50-Hz synchrony was significantly higher after rule shift errors than after errors during initial associations (Fig. 3i) or rule reversals (Fig. 3j). Notably, this difference was specific for 30–50 Hz.

Both rule shifts and rule reversals were uncued. Therefore, the nature of the rule change, and any associated differences in synchrony, should only become apparent over time. To confirm that this was the case, we analyzed trial-by-trial differences in gamma synchrony for incorrect versus correct trials, during rule shifts versus rule reversals. Indeed, the tendency for gamma synchrony to be higher on incorrect versus correct trials during rule shifts but not rule reversals was difficult to discern during the first two trials of a rule change and then became significantly larger over the next three trials (Extended Data Fig. 4k).

Note: we quantified synchrony using the fraction of 1-s time windows for which the R^2 between actual TEMPO signals exceeded that for 99% of time-shuffled signals. This bootstrapped metric is sparse in time. Therefore, we obtained a meaningful estimate of synchrony by averaging over many 1-s windows per trial and all trials of a given type—for example, time windows after errors including the following ITIs. As a consequence, our estimate of synchrony had low temporal resolution and cannot pinpoint specific moments of high synchrony. Rather, we can say only that synchrony tended

Fig. 2 | Cross-hemispheric gamma synchrony of PV interneurons increases after errors during rule shifts. a, *PV-Cre* Ai14 mice had bilateral AAV-DIO-Ace2N-4AA-mNeon ± AAV-Syn-tdTomato injections and fiber-optic implants in the mPFC. **b**, Representative images of tdTomato (red) and Ace-mNeon (green) fluorescence in a coronal section of mPFC (left), alongside a high-power image (right). Scale bars, 100 μm and 25 μm, respectively. **c**, Schematic for dual-site TEMPO measurements. Each fiber-optic implant, for delivering illumination and collecting fluorescence, connects to a mini-cube coupled to two LEDs and two photoreceivers (PRs) to separately excite and collect emitted fluorescence from Ace-mNeon and tdTomato. Two lock-in amplifiers modulate (mod.) LED output and demodulate PR signals, which are then acquired (acq.) by a multichannel real-time signal processor. **d**, Initial association (IA) and rule shift (RS) performance in this cohort ($n = 12$ mice). **e**, Overview of dual-site TEMPO analysis: tdTomato and Ace-mNeon fluorescence signals from each hemisphere (L, left; R, right) are filtered around a frequency of interest, and then both tdTomato signals and one Ace-mNeon signal are used to model the second Ace-mNeon signal. Performance is compared to models based on shuffled versions of the first Ace-mNeon signal. **f**, R^2 values, measuring zero-phase-lag ~40-Hz cross-hemispheric PV interneuron synchrony, during the last three IA trials and the first five RS trials in one mouse. **g**, Synchrony was not different after correct decisions versus during the baseline period ($n = 12$ mice; two-way ANOVA; condition × frequency interaction: $F_{2,33} = 1.05$, $P = 0.36$). **h**–**i**, 30–50-Hz synchronization was specifically higher after RS errors than during the baseline period ($n = 12$ mice; two-way ANOVA; main effect of condition: $F_{1,33} = 10.51$, $^{**}P = 0.003$; frequency × condition interaction: $F_{2,33} = 8.23$, $^{**}P = 0.001$; 15–25 Hz: post hoc $t_{(33)} = 0.43$, $P > 0.99$; 30–50 Hz: post hoc $t_{(33)} = 5.18$, $^{****}P = 0.00003$; 50–70 Hz: post hoc $t_{(33)} = 0.007$, $P > 0.99$) or after RS correct decisions ($n = 12$ mice; two-way ANOVA; condition × frequency interaction: $F_{2,33} = 7.32$, $^{**}P = 0.002$; post hoc $t_{(33)} = 4.36$, $^{***}P = 0.0004$). **j**, R^2 values, measuring zero-phase-lag ~40-Hz cross-hemispheric Sst interneuron synchrony during the last three IA trials and the first five RS trials in one mouse. **k**–**m**, Cross-hemispheric Sst synchrony ($n = 5$ mice) was not different between the baseline period and RS correct trials (two-way ANOVA; main effect of condition: $F_{1,12} = 0.07$, $P = 0.79$; main effect of frequency: $F_{2,12} = 6.07$, $^{*}P = 0.015$; condition × frequency interaction $F_{2,12} = 0.10$, $P = 0.90$), baseline period and RS incorrect trials (two-way ANOVA; main effect of condition: $F_{1,12} = 0.47$, $P = 0.51$; main effect of frequency: $F_{2,12} = 7.34$, $^{**}P = 0.008$; condition × frequency interaction: $F_{2,12} = 0.26$, $P = 0.78$), nor correct and incorrect trials (two-way ANOVA; main effect of condition: $F_{1,12} = 0.25$, $P = 0.63$; main effect of frequency: $F_{2,12} = 4.66$, $^{*}P = 0.03$; condition × frequency interaction: $F_{2,12} = 0.034$, $P = 0.97$). **n**, In a cohort of *PV-Cre* mice used for simultaneous dual-site TEMPO measurements and LFP recordings ($n = 5$ mice), 30–50-Hz synchronization between left and right PV interneuron TEMPO signals was specifically higher after RS errors than after RS correct decisions (two-way ANOVA; frequency × condition interaction: $F_{2,12} = 7.13$, $^{**}P = 0.009$; post hoc $t_{(12)} = 2.83$, $^{*}P = 0.045$). **o**, Difference in zero-phase-lag LFP wavelet coherence after errors relative to after correct decisions (that is, incorrect minus correct; $n = 5$ mice). **p**, LFP wavelet coherence was higher at 20 and 40 Hz after RS errors than after correct decisions ($n = 5$ mice; two-way ANOVA; main effect of condition: $F_{1,12} = 21.40$, $^{***}P = 0.0006$; main effect of frequency: $F_{2,12} = 1.86$, $P = 0.199$; condition × frequency: $F_{2,12} = 0.17$, $P = 0.85$; 20 Hz: post hoc $t_{(12)} = 2.85$, $^{*}P = 0.04$; 40 Hz: post hoc $t_{(12)} = 2.96$, $^{*}P = 0.04$). Data are shown as means (**d**, **o**); error bars denote s.e.m. Two-way ANOVA followed by Bonferroni post hoc comparisons was used unless otherwise noted. Comparisons were not significant unless otherwise noted.

to be higher during a set of time windows—for example, those after errors. This makes it difficult to link moments of high synchrony to specific behaviors—for example, digging or immobility. Nevertheless, when we restricted our analysis to time windows that fell during ITIs, cross-hemispheric PV interneuron gamma synchrony was higher during ITIs after rule shift errors than ITIs after initial association or rule reversal errors (Extended Data Fig. 4l). This indicates that increased gamma synchrony was not just a direct byproduct of specific movements or events occurring during the trial period but rather reflects feedback from the previous trial.

We cannot fully rule out that feedback from the previous trial altered ITI behavior in ways that mediate increased gamma synchrony. However, we consider this unlikely because behavior was not grossly different during ITIs after rule shift errors versus those after initial association errors. We scored videos of ITI behavior. These were of limited quality because the camera was focused on the test cage, not the holding cage, and the holding cage was partially covered by a translucent lid. Therefore, our analysis assessed only whether mice moved from one part of the cage to another. The fraction of timepoints spent moving was almost identical during ITIs after rule shift or initial association errors (rule shift, 68% moving, versus initial association, 70% moving; Extended Data Fig. 4m,n).

We also analyzed PV photometry signals during ITIs (Extended Data Fig. 1f). During rule shifts, these were higher for ITIs after

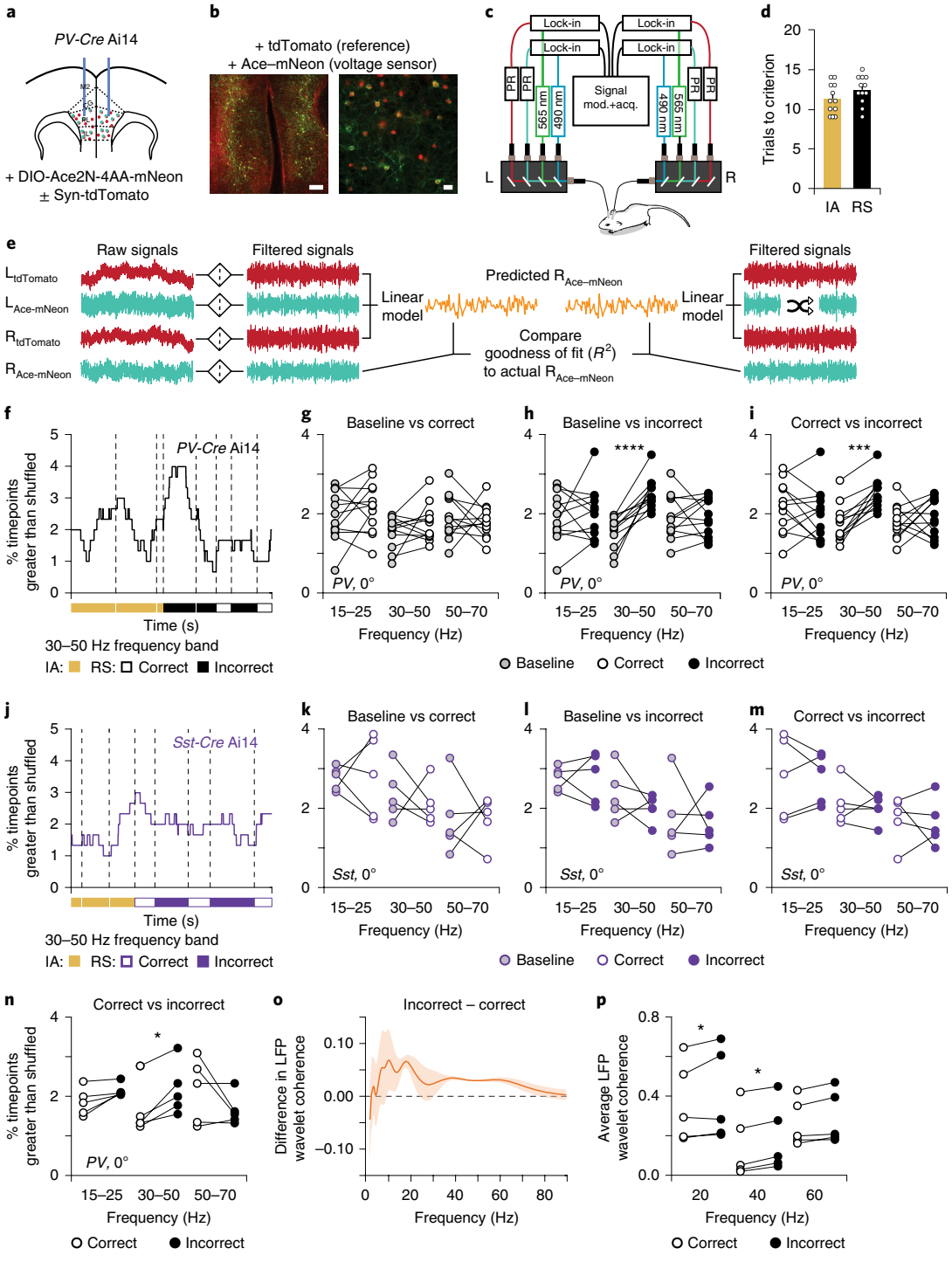

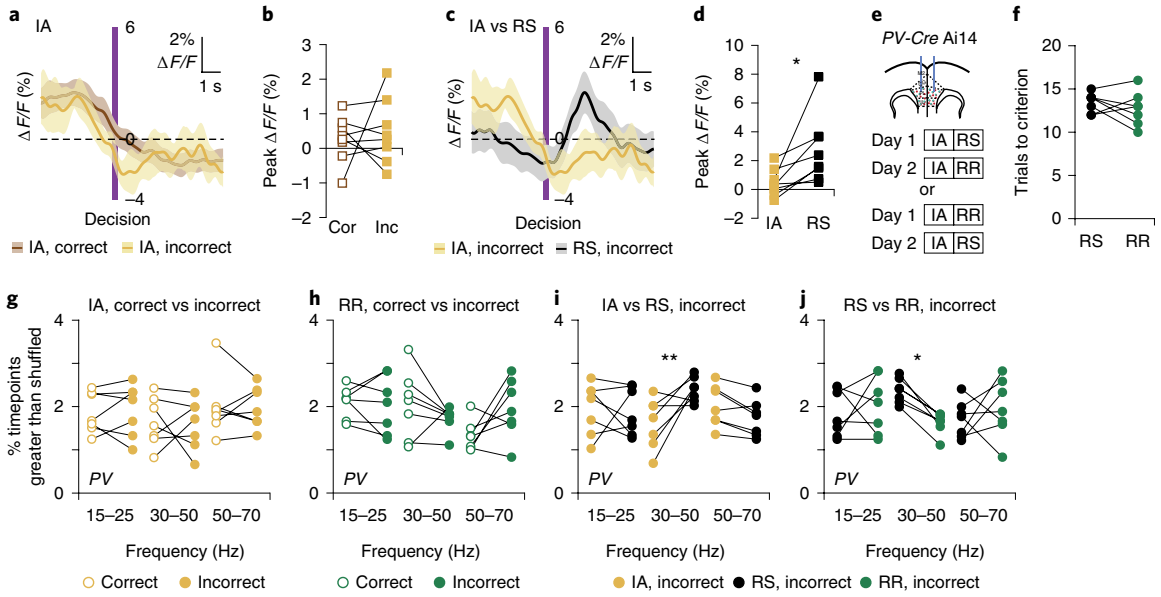

Fig. 3 | Cross-hemispheric synchrony does not increase during initial associations and rule reversals. a, Averaged PV interneuron photometry signal ($\Delta F/F$), aligned to the time of dig, which indicates a decision, for correct (brown line) and incorrect trials (yellow line) during the initial association (IA) ($n=8$ mice). **b**, Peak $\Delta F/F$ during the 4 s after the decision. Signals are similar during correct and incorrect IA trials ($n=8$ mice; two-tailed paired t-test; $t_{(7)}=0.44$, $P=0.67$). **c**, Averaged PV interneuron photometry signal ($\Delta F/F$), aligned to the time of dig, which indicates a decision, for incorrect trials during the IA (yellow line) or rule shift (RS) (black line; $n=8$ mice). **d**, Peak $\Delta F/F$ during the 4 s after the decision. Signals on incorrect trials are significantly lower during the IA than the RS ($n=8$ mice; two-tailed paired t-test; $t_{(7)}=2.87$, $^*P=0.024$). (Note: to be conservative and include all data, we did not exclude one datapoint that appeared to be an outlier; however, had this datapoint been excluded, this P value would have been 0.0096). **e**, *PV-Cre* Ai14 mice had bilateral injections of AAV-DIO-Ace2N-4AA-mNeon + AAV-Syn-tdTomato in the mPFC and fiber-optic implants in the mPFC. Experimental design: day 1: IA followed by RS or RR; day 2: IA followed by the task not performed on day 1. **f**, *PV-Cre* Ai14 mice performed RSs and RRs in a similar number of trials ($n=7$ mice; two-tailed paired t-test; $t_{(6)}=0.92$, $P=0.39$). **g**, During the IA, synchrony did not differ after correct versus incorrect trials ($n=7$ mice; two-way ANOVA; main effect of condition: $F_{1,18}=0.0007$, $P=0.98$; condition × frequency interaction: $F_{2,18}=0.068$, $P=0.93$). **h**, During the RR, synchrony did not differ after correct versus incorrect trials ($n=7$ mice; two-way ANOVA; main effect of condition: $F_{1,18}=0.10$, $P=0.76$; condition × frequency interaction $F_{2,18}=4.55$, $^*P=0.025$; 15–25 Hz: post hoc $t_{(18)}=0.25$, $P>0.99$; 30–50 Hz: post hoc $t_{(18)}=1.71$, $P=0.32$; 50–70 Hz: post hoc $t_{(18)}=2.50$, $P=0.07$). **i**, After errors, synchrony was specifically higher for the 30–50-Hz band during RS than IA ($n=7$ mice; two-way ANOVA; condition × frequency interaction: $F_{2,18}=6.02$, $^{**}P=0.0099$; 30–50 Hz: post hoc $t_{(18)}=3.42$, $^{**}P=0.009$). **j**, After errors, synchrony was specifically higher in the 30–50-Hz band during RS than RR (two-way ANOVA; condition × frequency interaction $F_{2,18}=3.96$, $^*P=0.038$; 30–50 Hz: post hoc $t_{(18)}=2.64$, $^*P=0.0499$). Data are shown as means (**a**, **c**); shading denotes s.e.m. Two-way ANOVA followed by Bonferroni post hoc comparisons was used unless otherwise noted.

errors than correct trials. Notably, this was not the case during initial associations. Thus, increases in PV interneuron activity and gamma synchrony that occured after rule shift errors persisted into the subsequent ITI, when mice were in holding cages and task-related cues were absent. Finally, although we could not pinpoint specific moments of high synchrony as outlined above, we did characterize behavior at the time of $\Delta F/F$ peaks, during both trials (Extended Data Fig. 1g) and ITIs (Extended Data Fig. 1h,i). During trials, peak PV interneuron activity was not consistently associated with any specific behavior and could occur while mice were digging before removal of the non-chosen bowl or after bowl removal while mice were digging, moving or immobile. During ITIs, peak PV interneuron activity occurred during both movement and immobility, and the fraction of peaks associated with each condition did not differ between ITIs after initial association versus rule shift errors. Thus, peaks in PV activity were not driven by specific behaviors, and differences in PV activity during ITIs after rule shift versus initial association errors did not reflect gross differences in movement.

Perturbing gamma synchrony disrupts learning during rule shifts. To directly test the functional significance of increased synchrony after rule shift errors, we sought to artificially manipulate cross-hemispheric gamma synchronization between PV interneurons. We previously showed that 40-Hz stimulation of interneurons delivered in-phase across the left and right mPFC does not impair rule shifts in normal mice[14]. Critically, whereas others have examined behavioral effects of 40-Hz stimulation of PV interneurons using light powers of ~5–7 mW[22,24], we used ~1 mW. Light power is not the only determinant of optogenetic efficacy, as ChR2 expression varies. Nevertheless, another study that stimulated PV interneurons at 40 Hz using ~1 mW observed only slight changes in excitatory neuron firing rates[23]. Thus, one strategy would be using modest optogenetic stimulation to entrain PV interneurons in the left versus right mPFC with different phase relationships to determine whether these patterns, which should elicit similar changes in levels of inhibition but differentially affect cross-hemispheric synchronization, produce similar versus distinct behavioral effects.

Based on this, we performed two experiments. First, stimulating prefrontal PV interneurons at 40 Hz but out-of-phase between hemispheres disrupted rule shift learning (Fig. 4a–e). Mice receiving out-of-phase stimulation took significantly longer to learn compared either to control (eYFP-expressing) mice or to themselves on a different day with no stimulation. Because odor–texture pairings vary randomly from trial to trial, during rule shifts mice can make perseverative and random errors. Perseverative errors occur when the originally rewarded cue and the newly rewarded cue are in different bowls, and the mouse chooses the originally rewarded one. Random errors occur when the originally rewarded and newly

rewarded cues are in the same bowl, but the mouse chooses the other bowl. Out-of-phase 40-Hz stimulation specifically increased perseverative errors (Fig. 4b,c and Extended Data Fig. 5a–f). Next, a different cohort of *PV-cre* mice underwent 1) out-of-phase 20-Hz stimulation, 2) out-of-phase 40-Hz stimulation, and 3) in-phase 40-Hz stimulation, delivered to PV interneurons in the left versus right mPFC during rule shifts (Fig. 4d). Out-of-phase 20-Hz stimulation did not disrupt rule shifts (Fig. 4e; compare to Fig. 2d). Again, out-of-phase 40-Hz stimulation markedly disrupted rule shift learning and increased perseveration, but when we delivered in-phase 40-Hz stimulation the next day, the same mice again learned normally (Fig. 4e and Extended Data Fig. 5g–i). This phenomenon was specific to PV interneurons: stimulating Sst interneurons out-of-phase (at 20 or 40 Hz) did not affect rule shifts (Extended Data Fig. 6).

To clarify how these patterns of optogenetic stimulation affect microcircuit activity, first we recorded from mPFC using silicon probes in head-fixed *PV-Cre* mice injected with virus for Cre-dependent ChR2 expression during 40-Hz PV interneuron stimulation (using the same light power as our behavioral experiments). Putative PV interneurons were single units with fast-spiking waveforms and reliable short-latency responses to stimulation (eight of ten fast-spiking units met our criteria)[30]. Stimulation strongly entrained 'optogenetically tagged' PV interneurons (Extended Data Fig. 7). Stimulation also entrained regular-spiking neurons but only modestly suppressed their overall spike rate (4.87 ± 0.35 versus 4.07 ± 0.33 spikes per s before versus during stimulation, respectively; $n = 237$ cells). A second experiment recorded LFPs from the mPFC in freely moving *PV-Cre* mice injected with virus to drive Cre-dependent ChR2 expression, while delivering 40-Hz optogenetic stimulation, either in-phase or out-of-phase between hemispheres (Extended Data Fig. 8). (We also recorded while delivering light in control ChR2-negative mice). Both patterns produced a slight bump at ~40 Hz and suppressed high-frequency (60–200 Hz) activity (relative to baseline recordings without stimulation). This suppression, which likely reflects the ability of optogenetically evoked inhibition to reduce overall mPFC activity, was most prominent at frequencies higher than 150 Hz and similar in magnitude for in-phase versus out-of-phase stimulation.

Perturbing gamma synchrony does not affect initial associations or rule reversals. Given that gamma synchrony increased during rule shifts but not during initial associations or rule reversals, we wondered whether it is specifically necessary for rule shifts or whether perturbing gamma synchrony would also disrupt these other types of learning. To examine this, we stimulated prefrontal PV interneurons at 40 Hz but out-of-phase across the two hemispheres during initial associations or rule reversals. In contrast to its ability to disrupt rule shifts, out-of-phase 40-Hz stimulation did not affect learning during initial associations or rule reversals (Fig. 4f–h). Unlike initial associations or rule reversals, rule shifts require mice to stop using one set of cues and to, instead, learn a new association that reappraises the behavioral significance of cues that were previously irrelevant to the outcome of each trial. In fact, once mice learned an initial association and rule shift, out-of-phase 40-Hz stimulation did not disrupt the ability of mice to revert to the original rule (Extended Data Fig. 9). For this, we switched back to

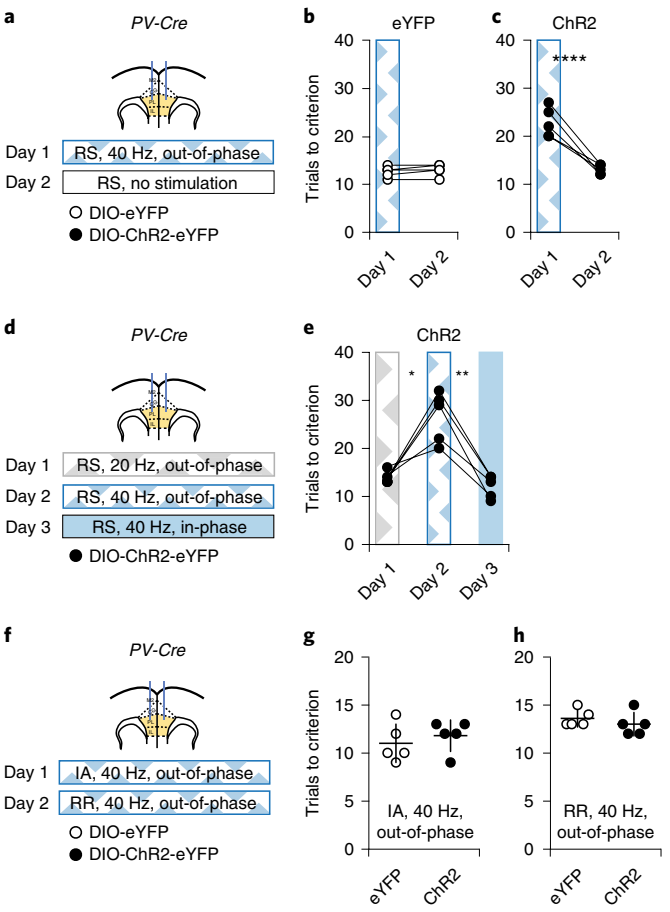

Fig. 4 | Out-of-phase, but not in-phase, gamma-frequency stimulation of PV interneurons disrupts learning during rule shifts but not during initial associations or rule reversals. a, *PV-Cre* Ai14 mice had injections of AAV-DIO-eYFP or AAV-DIO-ChR2-eYFP in the mPFC and fiber-optic implants bilaterally in the mPFC. Experimental design: day 1, out-of-phase 40-Hz stimulation during the rule shift (RS); day 2, no stimulation. **b**, **c**, Out-of-phase 40-Hz stimulation impairs rule shift performance in ChR2-expressing mice compared to eYFP-expressing controls ($n = 5$ mice in each cohort; two-way ANOVA; main effect of day: $F_{1,8} = 40.2$, $^{***}P = 0.0002$; main effect of virus: $F_{1,8} = 32.5$, $^{***}P = 0.0005$; day × virus interaction: $F_{1,8} = 47.3$, $^{***}P = 0.0001$). **b**, Performance of eYFP-expressing controls did not change from day 1 to day 2 ($n = 5$ mice; post hoc $t_{(8)} = 0.38$, $P > 0.99$). **c**, Out-of-phase 40-Hz stimulation of PV interneurons across hemispheres during the RS on day 1 impaired rule shifts in ChR2-expressing mice, compared to no stimulation on day 2 ($n = 5$ mice; post hoc $t_{(8)} = 9.34$, $^{****}P = 0.00003$). **d**, *PV-Cre* mice had bilateral injections of AAV-DIO-ChR2-eYFP and fiber-optic implants in the mPFC. Experimental design: day 1, out-of-phase 20-Hz stimulation; day 2, out-of-phase 40-Hz stimulation; day 3, in-phase 40-Hz stimulation. **e**, Out-of-phase 40-Hz stimulation (day 2) impairs rule shifts relative to out-of-phase 20-Hz stimulation (day 1) or in-phase 40-Hz stimulation (day 3) ($n = 5$ mice; one-way repeated measures ANOVA followed by Tukey's multiple comparisons test, main effect of treatment: $F_{1.294,5.175} = 25.3$, $^{**}P = 0.003$; day 1 versus day 2: $^{*}P = 0.025$, day 2 versus day 3: $^{**}P = 0.006$, day 1 versus day 3: $P = 0.47$). **f**, *PV-Cre* Ai14 mice had bilateral injections of AAV-DIO-eYFP or AAV-DIO-ChR2-eYFP and fiber-optic implants in the mPFC. Experimental design: day 1, out-of-phase 40-Hz stimulation during the initial association (IA); day 2, no stimulation during the IA, followed by out-of-phase 40-Hz stimulation during the rule reversal (RR). **g**, Out-of-phase 40-Hz stimulation does not affect the ability of ChR2-expressing mice to learn an IA ($n = 5$ mice in each cohort; two-tailed, unpaired *t*-test; compared to control eYFP-expressing mice; $t_{(8)} = 0.69$, $P = 0.51$). **h**, Out-of-phase 40-Hz stimulation does not affect the ability of ChR2-expressing mice to learn a RR ($n = 5$ mice in each cohort; two-tailed unpaired *t*-test; compared to control eYFP-expressing mice; $t_{(8)} = 0.89$, $P = 0.40$). Data are shown as means (**g**, **h**); error bars denote s.e.m. Two-way ANOVA followed by Bonferroni post hoc comparisons was used unless otherwise noted.

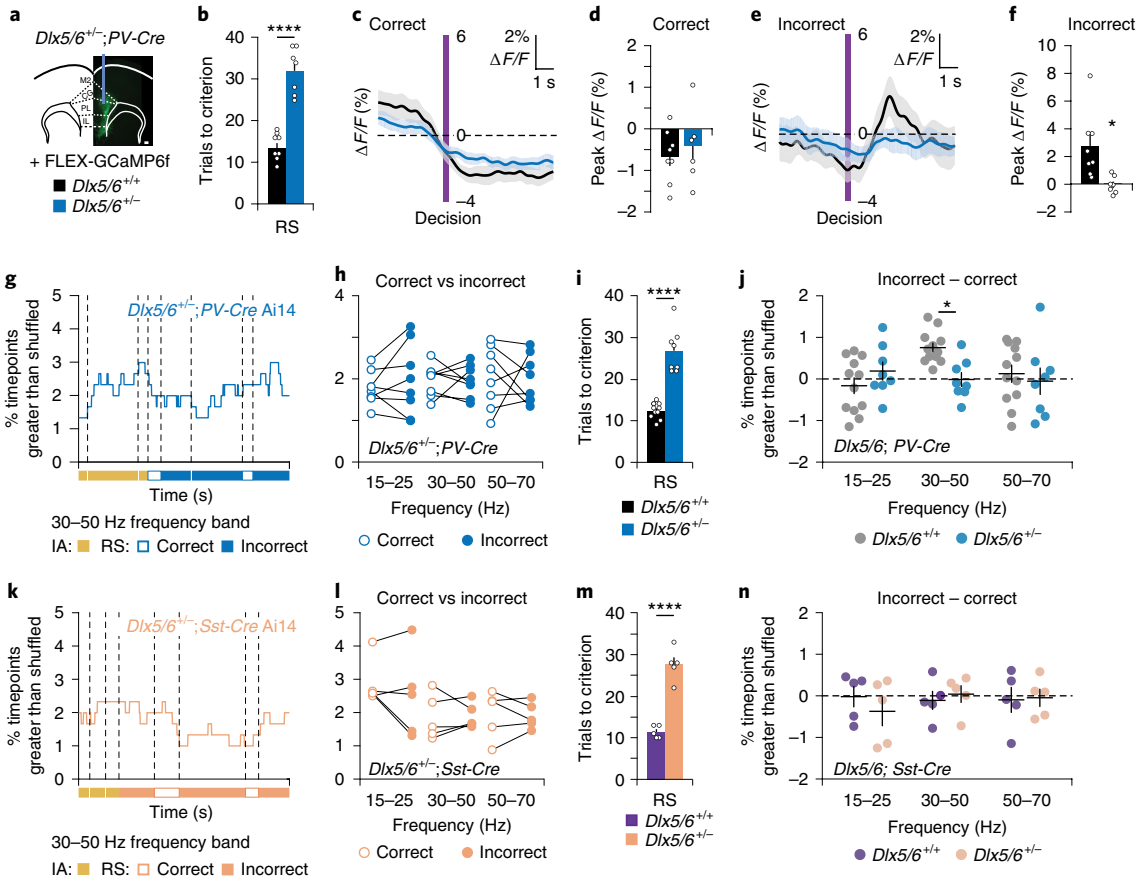

Fig. 5 | Cross-hemispheric gamma synchrony fails to increase during rule shifts in mutant mice. a, Representative FLEX-GCaMP6f expression in a *Dlx5/6*$^{+/-}$*;PV-Cre* mouse (scale bar, 100 µm). **b**, Rule shift (RS) performance is impaired in mutant mice (blue; $n=7$ mice) compared to wild-type (*Dlx5/6*$^{+/+}$) littermates (black; $n=8$ mice; two-tailed unpaired *t*-test; $t_{(13)}=7.82$, $^{****}P=0.000003$). **c**, Averaged $\Delta F/F$ from PV interneurons in mutant (blue; $n=7$ mice) versus wild-type (black; $n=8$ mice) mice, aligned to the time of correct decisions. **d**, Peak PV interneuron $\Delta F/F$ values during the 4 s after correct decisions during rule shifts were similar in *Dlx5/6*$^{+/-}$ (blue; $n=7$ mice) versus wild-type (black; $n=8$ mice; two-tailed unpaired *t*-test; $t_{(13)}=0.79$, $P=0.44$). **e**, Averaged $\Delta F/F$ from PV interneurons in mutant (blue; $n=7$ mice) versus wild-type (black; $n=8$ mice), aligned to the time of incorrect decisions. **f**, Peak $\Delta F/F$ from PV interneurons during the 4 s after incorrect decisions is significantly decreased in *Dlx5/6*$^{+/-}$ (blue; $n=7$ mice) compared to wild-type (black; $n=8$ mice) (two-tailed unpaired *t*-test; $t_{(8.085)}=3.18$, $^{*}P=0.01$). **g**, R^2 values, measuring zero-phase-lag ~40-Hz cross-hemispheric interneuron synchronization between TEMPO signals from PV interneurons in mutant mice during the last three IA and first five RS trials in one *Dlx5/6*$^{+/-}$ mouse. **h**, In *Dlx5/6*$^{+/-}$ mice, cross-hemispheric PV interneuron synchronization was not different after errors versus correct decisions ($n=8$ mice; two-way ANOVA; main effect of condition: $F_{1,21}=0.09$, $P=0.77$; condition × frequency interaction: $F_{2,21}=0.29$, $P=0.75$). **i**, Rule shift performance is impaired in mutant mice (blue; $n=8$ mice) compared to wild-type (black) littermates ($n=12$ mice; two-tailed unpaired *t*-test; $t_{(8.071)}=7.40$, $^{****}P=0.00007$). **j**, Increases in PV interneuron synchrony after errors (relative to synchrony after correct decisions) are significantly attenuated in mutants ($n=8$ mice) compared to wild-type littermates ($n=12$ mice), specifically in the 30–50-Hz frequency band (two-way ANOVA; genotype × frequency interaction: $F_{2,36}=3.98$, $^{*}P=0.028$; 15–25 Hz: post hoc $t_{(54)}=1.15$, $P=0.76$; 30–50 Hz: post hoc $t_{(54)}=2.67$, $^{*}P=0.03$; 50–70 Hz: post hoc $t_{(54)}=0.63$, $P>0.99$). **k**, R^2 values, measuring zero-phase-lag ~40-Hz cross-hemispheric Sst interneuron synchronization during the last three IA and first five RS trials in one *Dlx5/6*$^{+/-}$ mouse. **l**, In mutants ($n=5$ mice), cross-hemispheric Sst interneuron synchrony is similar after correct versus incorrect decisions (two-way ANOVA; main effect of condition: $F_{1,12}=0.70$, $P=0.42$; main effect of frequency: $F_{2,12}=2.16$, $P=0.16$; condition × frequency interaction: $F_{2,12}=0.71$, $P=0.51$). **m**, Rule shift performance is impaired in mutants ($n=5$ mice) compared to wild-type littermates ($n=5$ mice; two-tailed unpaired *t*-test; $t_{(8)}=8.64$, $^{****}P=0.00003$). **n**, Changes in Sst interneuron synchrony after errors (relative to synchrony after correct decisions) are not different in mutants ($n=5$ mice) versus wild-types ($n=5$ mice; two-way ANOVA; main effect of genotype: $F_{1,8}=0.06$, $P=0.82$; genotype × frequency interaction: $F_{2,16}=0.54$, $P=0.59$). Data are shown as means (**b**–**f**, **i**–**j**, **m**–**n**); error bars (**b**, **d**, **f**, **i**–**j**, **m**–**n**) and shading (**c**, **e**) denote s.e.m. Two-way ANOVA followed by Bonferroni post hoc comparisons was used unless otherwise noted.

the original rule (that is, initial association) after mice learned a rule shift and only delivered out-of-phase stimulation while switching back to the original rule. This provides additional confirmation that 40-Hz synchrony is specifically required for behavioral reappraisal, not generic forms of learning or switching.

Gamma synchrony fails to increase in mutant mice that exhibit perseveration. Finally, to evaluate how changes in gamma synchrony might contribute to, or be targeted to alleviate, pathological phenotypes, we exploited *Dlx5/6*$^{+/-}$ mice, which have abnormal PV interneurons, deficient task-evoked gamma oscillations and perseveration during rule shifts[14]. The error-related photometry signals normally observed in wild-type (*Dlx5/6*$^{+/+}$) PV interneurons during rule shifts were significantly attenuated in *Dlx5/6* mutants (Fig. 5e,f). By contrast, PV interneuron photometry signals after correct decisions were unaltered (Fig. 5c,d). In contrast to normal

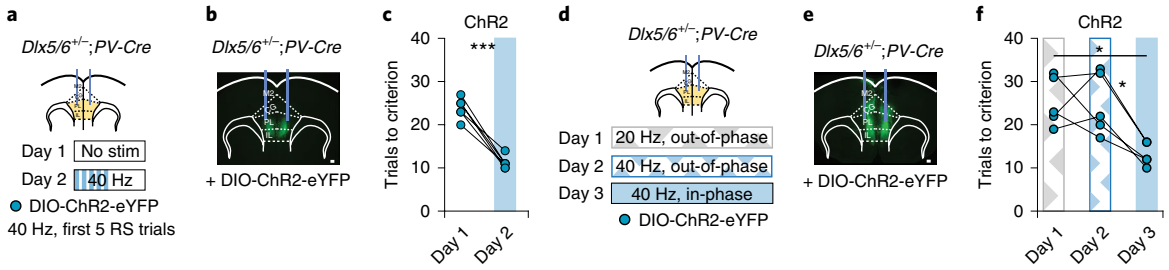

Fig. 6 | Restoring cross-hemispheric PV interneuron gamma synchrony is required to rescue rule shift performance in *Dlx5/6*$^{+/-}$ mutant mice. a, *Dlx5/6*$^{+/-}$*;PV-Cre* mice had bilateral AAV-DIO-ChR2-eYFP injections and fiber-optic implants in the mPFC. Experimental design: day 1, no stimulation; day 2, in-phase 40-Hz stimulation during the first five RS trials. **b**, Representative ChR2-eYFP expression in the mPFC of a *Dlx5/6*$^{+/-}$*;PV-Cre* mouse (scale bar, 100 μm). **c**, In-phase 40-Hz stimulation on day 2 normalizes rule shift performance in mutant mice ($n = 6$ mice; two-tailed paired *t*-test; $t_{(5)} = 10.3$, $^{***}P = 0.0001$). **d**, *Dlx5/6*$^{+/-}$*;PV-Cre* mice had bilateral AAV-DIO-ChR2-eYFP injections and fiber-optic implants in the mPFC. Experimental design: day 1, out-of-phase 20-Hz stimulation; day 2, out-of-phase 40-Hz stimulation; day 3, in-phase 40-Hz stimulation. **e**, Representative ChR2-eYFP expression in the mPFC of a *Dlx5/6*$^{+/-}$*;PV-Cre* mouse (scale bar, 100 μm). **f**, In mutants ($n = 5$ mice), in-phase 40-Hz stimulation (day 3), but not out-of-phase 40-Hz stimulation (day 2), rescues rule shift performance (one-way repeated-measures ANOVA followed by Tukey's multiple comparisons test, main effect of treatment: $F_{1.451,5.806} = 12.98$, $^{**}P = 0.009$; day 1 versus day 2: $P = 0.98$, day 2 versus day 3: $^{*}P = 0.016$, day 1 versus day 3: $^{*}P = 0.01$). Two-way ANOVA followed by Bonferroni post hoc comparisons was used unless otherwise noted.

mice, in mutants, 30–50-Hz cross-hemispheric synchronization was not higher after rule shift errors versus correct decisions (Fig. 5g–i and Extended Data Fig. 10b,i–l). Correspondingly, the normal increase in 30–50-Hz cross-hemispheric PV interneuron synchronization after rule shift errors (relative to correct trials) was significantly attenuated in *Dlx5/6*$^{+/-}$ mice compared to wild-types (Fig. 5j). This difference was specific for frequency (30–50 Hz versus 15–25 or 50–70 Hz), task (rule shift versus initial association or rule reversal) and cell type (PV versus Sst interneurons) (Fig. 5j, Extended Data Fig. 10q–s, Fig. 5k–n and Extended Data Fig. 10c,d,m–p).

Only in-phase gamma-frequency PV interneuron stimulation rescues perseveration. We previously found that 40-Hz stimulation of mPFC interneurons rescues learning during rule shifts in *Dlx5/6* mutant mice[14]. Our new results suggest that gamma synchrony between prefrontal PV interneurons during the early portions of a rule shift might be particularly critical for this effect. We tested this three ways. First, restricting optogenetic stimulation to only PV interneurons and just the first five rule shift trials was sufficient to rescue learning in *Dlx5/6* mutants (Fig. 6a–c and Extended Data Fig. 10e,f). Second, 20- or 40-Hz stimulation of PV interneurons that was out-of-phase between hemispheres did not improve rule shift learning in mutants (Fig. 6d–f and Extended Data Fig. 10g,h). However, consistent with our earlier findings[14], in-phase 40-Hz stimulation rescued their rule shift performance (Fig. 6f and Extended Data Fig. 10e–h). (Notably, without optogenetic stimulation, rule shift performance in *Dlx5/6* mutants did not improve over three consecutive days of testing[14].) These results show that gamma-frequency activity in prefrontlal PV interneurons was not sufficient to facilitate rule shifts unless it was precisely synchronized across hemispheres. Finally, in-phase 40-Hz stimulation bilateral stimulation of Sst interneurons did not improve rule shift performance in *Dlx5/6* mutants (Extended Data Fig. 6l–p).

A pro-cognitive pharmacological intervention specifically increases gamma synchrony. Optogenetic stimulation might be viewed as 'artificially' altering gamma synchrony. Therefore, we explored whether manipulations engaging endogenous physiological mechanisms also increase gamma synchrony and elicit similar behavioral effects. For this, we used low (sub-anxiolytic and sub-sedative) doses of the benzodiazepine clonazepam. We previously[14] showed that clonazepam (0.0625 mg kg^{-1}, intraperitoneally), like 40-Hz optogenetic stimulation, normalizes rule shifts in *Dlx5/6*$^{+/-}$ mice (we also reproduced that here: Fig. 7a–c). Now, using TEMPO, we found that clonazepam increased cross-hemispheric gamma synchrony between prefrontal PV interneurons in *Dlx5/6*$^{+/-}$ mice (Fig. 7d,e,h). This specifically occurred after rule shift errors (not at baseline period or after correct decisions) (Fig. 7f,g) and for 30–50 Hz (Fig. 7h).

Discussion

These results directly address longstanding controversies about the functional significance of synchronization across neuronal structures[7,8,11,18,31–33]. We found a double dissociation between therapeutic or disruptive effects elicited by in-phase versus out-of-phase stimulation. This confirms that certain aspects of behavior depend on cross-hemispheric gamma synchrony between PV interneurons, not just rhythmic inhibition in local circuits. Furthermore, in both stimulation and TEMPO experiments, gamma synchrony was not involved in generic aspects of learning, decision-making or flexibility but, rather, specifically contributed to behavioral reappraisal: the formation of new associations based on familiar cues that were previously irrelevant to behavioral outcomes. This study focused on normal behavior, but experiments in *Dlx5/6* mutant mice independently validated this relationship between gamma synchrony and behavioral reappraisal. Notably, this type of learning occurred without extensive prior training, differentiating it from the switching between well-learned behaviors that is commonly studied in mice. Learning that reappraises the salience of external cues is critical for adaptation to changing environments.

Extracting synchrony from genetically encoded voltage indicators. Several controls confirm that our method measures task-dependent changes in gamma-frequency synchronization between PV interneurons. Increased synchrony after errors is specific for 1) the gamma band, 2) rule shifts and 3) PV interneurons. If the increased synchrony that we observed was driven by non-neuronal artifacts or kinetics of Ace–mNeon, then it should have been present in both PV and Sst interneurons. If increased synchrony was driven by nonspecific aspects of PV neuron activity (as opposed to gamma-frequency activity), synchrony should have increased in other frequency bands. And if this increased synchrony was driven by nonspecific aspects of our task—for example, generic reward or error signals or movements mice make after errors—it should have been observed during rule reversals and initial associations (as well as rule shifts). Finally, increased gamma synchrony

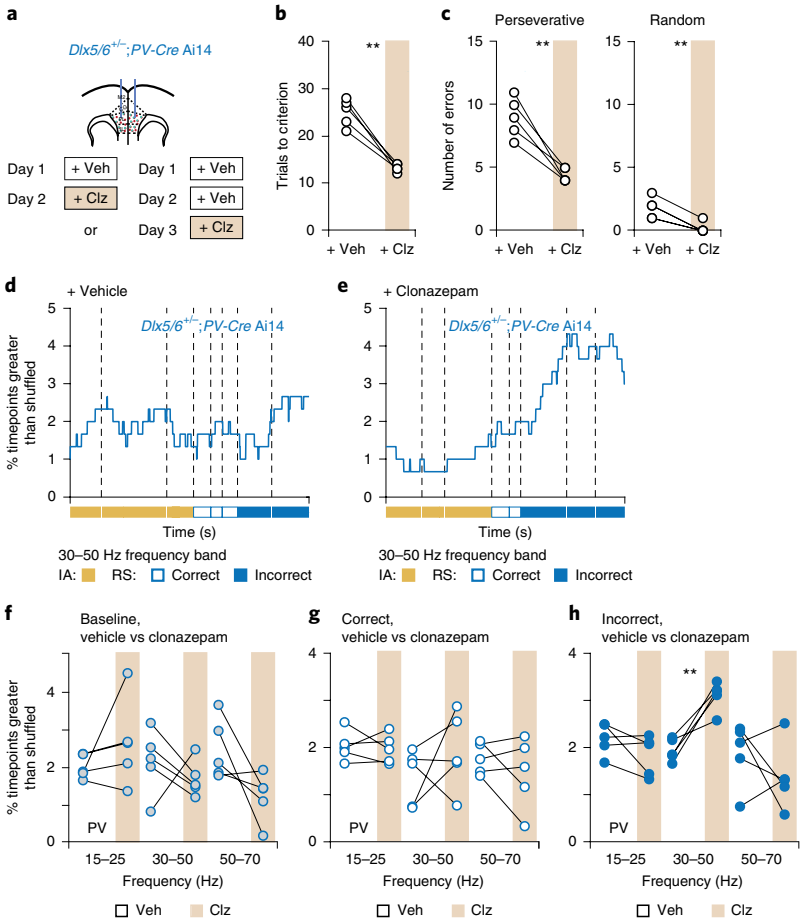

Fig. 7 | Low-dose clonazepam increases cross-hemispheric gamma synchrony during rule shifts in mutant mice. a, *Dlx5/6*$^{+/-}$*;PV-Cre* Ai14 mice ($n=5$ mice) had bilateral AAV-DIO-Ace2N-4AA-mNeon ± AAV-Syn-tdTomato injections and fiber-optic implants in the mPFC. Experimental design: all mice received vehicle only (veh) on day 1. On day 2, some mice received clonazepam (clz; $n=3$ mice); others received vehicle. On day 3, we administered clz to those mice that received veh on day 2 ($n=2$ mice). **b**, Low-dose clonazepam normalizes rule shift performance in mutants ($n=5$ mice; two-tailed paired *t*-test; $t_{(4)}=8.07$, $^{**}P=0.0013$). **c**, Low-dose clonazepam decreases perseverative and random errors ($n=5$ mice; two-tailed paired *t*-test; $t_{(4)}=6.15$, $^{**}P=0.0036$ for perseverative, $t_{(4)}=6.53$, $^{**}P=0.0028$ for random). **d**, R^2 values, measuring zero-phase-lag ~40-Hz cross-hemispheric interneuron synchronization between TEMPO signals from PV interneurons in one *Dlx5/6*$^{+/-}$ mouse, during the last three IA and first five RS trials, in the vehicle condition. **e**, R^2 values, measuring zero-phase-lag ~40-Hz cross-hemispheric interneuron synchronization between TEMPO signals from PV interneurons in the same mutant mouse, during the last three IA and first five RS trials in the clonazepam condition. **f**, During the baseline period, synchrony did not differ between the vehicle and clonazepam conditions ($n=5$ mice; two-way ANOVA; main effect of treatment: $F_{1,12}=1.37$, $P=0.26$; frequency × treatment interaction: $F_{2,12}=3.22$, $P=0.08$). **g**, Synchrony did not differ after correct trials in the vehicle and clonazepam conditions ($n=5$ mice; two-way ANOVA; main effect of treatment: $F_{1,12}=0.08$, $P=0.78$; interaction $F_{2,12}=1.60$, $P=0.24$; 15–25 Hz: post hoc $t_{(12)}=0.19$, $P>0.99$; 30–50 Hz: post hoc $t_{(12)}=1.57$, $P=0.43$; 50–70 Hz: post hoc $t_{(12)}=0.88$, $P>0.99$). **h**, After RS errors, synchrony was specifically higher in the clonazepam condition for the 30–50-Hz band ($n=5$ mice; two-way ANOVA; treatment × frequency interaction: $F_{2,12}=8.63$, $^{**}P=0.005$; 30–50 Hz: post hoc $t_{(12)}=3.73$, $^{**}P=0.009$). Two-way ANOVA followed by Bonferroni post hoc comparisons was used unless otherwise noted.

was observed only for in-phase Ace–mNeon signals, not when one Ace–mNeon signal was shifted 90 degrees out of phase (~6 ms). This confirms that this increased ability to predict one Ace–mNeon signal using the other reflects synchrony between these signals, not the fact that they have similar autocorrelations or higher-order statistics.

In addition to the negative controls described above, clonazepam enhanced gamma synchrony. This represents a positive control that our method is sensitive to manipulations known to enhance PV interneuron output and gamma oscillations.

LFPs and signals from genetically encoded voltage indicators (GEVIs) measure different things and are contaminated by distinct noise sources. Thus, there is not likely to be a 1:1 correspondence between them. Nevertheless, we used LFPs to validate the essence of our GEVI findings: cross-hemispheric LFPs exhibited increased gamma-frequency (~40 Hz) synchrony after incorrect trials, relative to correct ones, during rule shifts. The precise relationship between LFPs and GEVI signals remains an important topic for future studies.

Our current approach does not measure absolute levels of synchrony, because the variation in measurements across mice is high, making it necessary to perform some kind of within-mouse normalization. As a result, we cannot exclude the possibility that baseline gamma synchrony is elevated in *Dlx5/6* mutant mice (relative to normal *Dlx5/6*$^{+/+}$ mice), such that the failure of these mice to increase gamma synchrony during rule shifts reflects a ceiling effect. Another limitation is that, although GEVIs are ideal for measuring mesoscale patterns of activity within sparse cell types, our approach does not reveal how individual neurons might encode information via the phase of their firing. Finally, although it might be possible to

detect action potentials by specifically imaging the soma of neurons, bulk measurements from voltage indicators should be dominated by subthreshold signals, for two reasons. First, spikes are very brief compared to subthreshold oscillations. Second, most neuronal surface area is located in the dendrites (~96% for PV interneurons[34]), and spike propagation into PV interneuron dendrites is poor[35].

The significance of zero-phase-lag synchronization. Increases in gamma synchrony occurred for simultaneously recorded Ace–mNeon signals but not when one signal was shifted 90 degrees out of phase. This indicates that the population-level phase lag is near zero. This might seem puzzling, because synaptic communication between the hemispheres involves time delays that are commonly assumed to produce phase differences. In fact, zero-phase-lag synchrony commonly emerges in bidirectionally coupled oscillators, even when they communicate with significant delays. Consider two phase oscillators, representing the hemispheres, which emit output (spikes) upon completing each cycle. Assume this output reaches the other oscillator after a quarter-cycle delay (~6 ms for 40 Hz), perturbing the phase of the post-synaptic oscillator proportional to the cosine of its current phase. (Such coupling is not hard to imagine: suppose that output arriving when excitatory neuron firing approaches its peak recruits more excitation, accelerating the next cycle, whereas output arriving later, when inhibitory neurons have been recruited, mainly increases inhibition, delaying the next cycle.) For weak coupling, this system exhibits zero-phase-lag synchrony, even though these two oscillators communicate with a quarter-cycle delay.

Another potential concern is about the function of zero-phase-lag synchrony. We previously showed that inputs modulated at gamma frequency transmit greater information to downstream neurons than non-rhythmic inputs[9]. Suppose that the left and right mPFC converge on a common downstream target. Then, when they are synchronized with zero-phase lag, inputs from the left and right mPFC hemispheres will summate in downstream neurons in a manner preserving the gamma-frequency modulation within each individual signal. By contrast, when activity is out of phase between hemispheres, the rhythmic modulation of their summated input will be degraded, compromising information transmission to downstream targets. Thus, cross-hemispheric gamma synchrony might potentiate prefrontal outputs to other regions that serve to update the behavioral salience of external cues. Indeed, we observed that 40-Hz optogenetic stimulation of PV interneurons strongly entrained regular spiking units. An important future direction is determining whether specific classes of prefrontal pyramidal neurons, projecting to particular targets, exhibit increased gamma synchrony during rule shifts. This might be true for projections to the dorsomedial striatum, nucleus accumbens and/or mediodorsal thalamus, because these projections are important for cognitive flexibility[15,36,37], and PV interneurons strongly inhibit mPFC neurons that project bilaterally to these structures[38].

Whatever the function of cross-hemispheric synchrony is, it is specific for synchrony at ~40 Hz, as optogenetically disrupting 20-Hz synchronization did not disrupt rule shift performance. The simplest explanation for this is that out-of-phase 20-Hz stimulation does not prevent PV interneurons from synchronizing at frequencies of ~40 Hz. Indeed, the previously described coupled oscillators, which normally synchronize at 40 Hz, continue to do so even when receiving simulated out-of-phase stimulation at half their natural frequency (that is, 10-ms pulses at 20 Hz).

Optogenetically perturbing synchrony. Optogenetic stimulation and inhibition are commonly used to test the causal significance of specific patterns of neural activity. However, optogenetic manipulations induce firing that is, by definition, 'artificial.' Several observations indicate that our optogenetic results inform normal circuit function, rather than simply inducing non-physiological states. First, we used modest optogenetic stimulation that we and others found did not markedly alter overall levels of circuit activity. Second, we delivered exactly the same pattern of stimulation to each PFC, either in phase or out of phase, and behavior was completely normal during in-phase stimulation. Thus, the disruptive effects of out-of-phase stimulation cannot be attributed to excessive PV interneuron firing or hypersynchrony within one hemisphere. Rather, the disruption of rule shifts must reflect the induction of artificial (nonzero) phase differences.

Finally, in-phase stimulation, which does not affect behavior in normal mice, rescues rule shift performance in mutant mice. This same effect can be produced using sub-anxiolytic and sub-sedative doses of clonazepam[14], which also restore increases in gamma synchrony normally seen in wild-type mice after rule shift errors. This suggests that in-phase stimulation is functionally similar to clonazepam, which acts by enhancing endogenous PV interneuron output. Thus, in-phase stimulation might reproduce physiologically and therapeutically relevant states, rather than creating aberrant ones. In this way, optogenetic experiments reveal how specific aspects of normally occurring activity (zero-phase-lag cross-hemispheric gamma synchrony between PV interneurons) contribute to behavior.

Clinical relevance. Disruptions in PV interneurons and gamma synchrony[39–41] are hypothesized to contribute to cognitive deficits at the core of schizophrenia[42,43]. Deficits in PV interneurons and gamma synchrony might also contribute to cognitive deficits in Alzheimer's disease[44], and driving synchronized gamma oscillations might ameliorate behavioral and neuropathological aspects of this disorder[45,46]. Our findings suggest that interventions that restore gamma oscillations might treat cognitive deficits but only when they involve the proper cell types and reproduce endogenous patterns of synchronization.

In individuals at high risk for psychosis, deficits in the ability to learn new associations based on previously irrelevant cues are strongly correlated with impairments in insight, which is the capacity to appraise and modify distorted beliefs about anomalous experiences[47]. Impaired insight plays a central role in the development and maintenance of psychosis[48]. This suggests that gamma synchrony might be relevant to psychosis itself (not just cognitive dysfunction) in schizophrenia.

Online content

Any methods, additional references, Nature Research reporting summaries, source data, extended data, supplementary information, acknowledgements, peer review information; details of author contributions and competing interests; and statements of data and code availability are available at https://doi.org/10.1038/s41593-020-0647-1.

Received: 7 June 2019; Accepted: 22 April 2020;
Published online: 25 May 2020

References

1. Young, D. A., Davila, R. & Scher, H. Unawareness of illness and neuropsychological performance in chronic schizophrenia. *Schizophr. Res.* **10**, 117–124 (1993).
2. Shad, M. U., Tamminga, C. A., Cullum, M., Haas, G. L. & Keshavan, M. S. Insight and frontal cortical function in schizophrenia: a review. *Schizophr. Res.* **86**, 54–70 (2006).
3. von der Malsburg, C. *The Correlation Theory of Brain Function* http://cogprints.org/1380/ (1981).
4. Abeles, M., Prut, Y., Bergman, H. & Vaadia, E. Synchronization in neuronal transmission and its importance for information processing. *Prog. Brain Res.* **102**, 395–404 (1994).
5. Singer, W. Neuronal synchrony: a versatile code for the definition of relations? *Neuron* **49**, 111–125 (1999).
6. Salinas, E. & Sejnowski, T. J. Correlated neuronal activity and the flow of neural information. *Nat. Rev. Neurosci.* **8**, 539–550 (2011).

7. Fries, P. A mechanism for cognitive dynamics: neuronal communication through coherence. *Trends Cogn. Sci.* **9**, 474–480 (2005).
8. Fries, P. Neuronal gamma-band synchronization as a fundamental process in cortical computation. *Annu. Rev. Neurosci.* **32**, 209–224 (2009).
9. Sohal, V. S., Zhang, F., Yizhar, O. & Deisseroth, K. Parvalbumin neurons and gamma rhythms enhance cortical circuit performance. *Nature* **459**, 698–702 (2009).
10. Fries, P. Rhythms for cognition: communication through coherence. *Neuron* **88**, 220–235 (2015).
11. Sohal, V. S. How close are we to understanding what (if anything) gamma oscillations do in cortical circuits? *J. Neurosci.* **36**, 10489–10495 (2016).
12. Bastos, A. M., Loonis, R., Kornblith, S., Lundqvist, M. & Miller, E. K. Laminar recordings in frontal cortex suggest distinct layers for maintenance and control of working memory. *Proc. Natl Acad. Sci. USA.* **115**, 1117–1122 (2018).
13. Miller, E. K., Lundqvist, M. & Bastos, A. M. Working memory 2.0. *Neuron* **100**, 463–475 (2018).
14. Cho, K. K. A. et al. Gamma rhythms link prefrontal interneuron dysfunction with cognitive inflexibility in *Dlx5/6*$^{+/-}$ mice. *Neuron* **85**, 1332–1343 (2015).
15. Marton, T. F., Seifikar, H., Luongo, F. J., Lee, A. T. & Sohal, V. S. Roles of prefrontal cortex and mediodorsal thalamus in task engagement and behavioral flexibility. *J. Neurosci.* **38**, 2569–2578 (2018).
16. Karlsson, M. P., Tervo, D. G. & Karpova, A. Y. Network resets in medial prefrontal cortex mark the onset of behavioral uncertainty. *Science* **338**, 135–139 (2012).
17. Cardin, J. A. Snapshots of the brain in action: local circuit interactions through the lens of gamma oscillations. *J. Neurosci.* **36**, 10496–10504 (2016).
18. Ray, S. & Maunsell, J. H. Do gamma oscillations play a role in cerebral cortex? *Trends Cogn. Sci.* **19**, 78–85 (2015).
19. Bissonette, G. B. et al. Double dissociation of the effects of medial and orbital prefrontal cortical lesions on attentional and affective shifts in mice. *J. Neurosci.* **28**, 11124–11130 (2008).
20. Ellwood, I. T. et al. Tonic or phasic stimulation of dopaminergic projections to prefrontal cortex causes mice to maintain or deviate from previously learned behavioral strategies. *J. Neurosci.* **37**, 8315–8329 (2017).
21. Canetta, S. et al. Maternal immune activation leads to selective functional deficits in offspring parvalbumin interneurons. *Mol. Psychiatry* **21**, 956–968 (2016).
22. Cao, W. et al. Gamma oscillation dysfunction in mPFC leads to social deficits in neuroligin 3 R451C knockin mice. *Neuron* **97**, 1253–1260 (2018).
23. Siegle, J. H., Pritchett, D. L. & Moore, C. I. Gamma-range synchronization of fast-spiking interneurons can enhance detection of tactile stimuli. *Nat. Neurosci.* **17**, 1371–1379 (2014).
24. Kim, H., Ahrlund-Richter, S., Wang, X., Deisseroth, K. & Carlén, M. Prefrontal parvalbumin neurons in control of attention. *Cell* **164**, 208–218 (2016).
25. Gunaydin, L. A. et al. Natural neural projection dynamics underlying social behavior. *Cell* **157**, 1535–1551 (2014).
26. Lerner, T. N. et al. Intact-brain analyses reveal distinct information carried by SNc dopamine subcircuits. *Cell* **162**, 635–647 (2015).
27. Chen, T. W. et al. Ultrasensitive fluorescent proteins for imaging neuronal activity. *Nature* **499**, 295–300 (2013).
28. Marshall, J. D. et al. Cell-type-specific optical recording of membrane voltage dynamics in freely moving mice. *Cell* **167**, 1650–1662 (2016).
29. Carandini, M. et al. Imaging the awake visual cortex with a genetically encoded voltage indicator. *J. Neurosci.* **35**, 53–63 (2015).
30. Pi, H. J. et al. Cortical interneurons that specialize in disinhibitory control. *Nature* **7477**, 521–524 (2013).
31. Ray, S., Ni, A. M. & Maunsell, J. H. Strength of gamma rhythm depends on normalization. *PLoS Biol.* **11**, e1001477 (2013).
32. Shadlen, M. N. & Movshon, J. A. Synchrony unbound: a critical evaluation of the temporal binding hypothesis. *Neuron* **24**, 67–77 (1999).
33. Palmigiano, A., Geisel, T., Wolf, F. & Battaglia, D. Flexible information routing by transient synchrony. *Nat. Neurosci.* **7**, 1014–1022 (2017).
34. Tukker, J. J. et al. Distinct dendritic arborization and in vivo firing patterns of parvalbumin-expressing basket cells in the hippocampal area CA3. *J. Neurosci.* **33**, 6809–6825 (2013).
35. Hu, H., Gan, J. & Jonas, P. Fast-spiking, parvalbumin^{+} GABAergic interneurons: from cellular design to microcircuit function. *Science* **345**, 1255263 (2014).
36. Otis, J. M. et al. Prefrontal cortex output circuits guide reward seeking through divergent cue encoding. *Nature* **543**, 103–107 (2017).
37. Bissonette, G. B. & Roesch, M. R. Neurophysiology of rule switching in the corticostriatal circuit. *Neuroscience* **345**, 64–76 (2017).
38. Phillips, E. A. K. & Hasenstaub, A. R. Asymmetric effects of activating and inactivating cortical interneurons. *eLife* **5**, e18383 (2016).
39. Gonzalez-Burgos, G., Cho, R. Y. & Lewis, D. A. Alterations in cortical network oscillations and parvalbumin neurons in schizophrenia. *Biol. Psychiatry* **77**, 1031–1040 (2015).
40. Uhlhaas, P. J. & Singer, W. Oscillations and neuronal dynamics in schizophrenia: the search for basic symptoms and translational opportunities. *Biol. Psychiatry* **77**, 1001–1009 (2015).
41. Senkowski, D. & Gallinat, J. Dysfunctional prefrontal gamma-band oscillations reflect working memory and other cognitive deficits in schizophrenia. *Biol. Psychiatry* **77**, 1010–1019 (2015).
42. Green, M. J. Cognitive impairment and functional outcome in schizophrenia and bipolar disorder. *J. Clin. Psych.* **67**, 36–42 (2006).
43. Minzenberg, M. J. & Carter, C. S. Developing treatments for impaired cognition in schizophrenia. *Trends Cogn. Sci.* **16**, 35–42 (2012).
44. Verret, L. et al. Inhibitory interneuron deficit links altered network activity and cognitive dysfunction in Alzheimer model. *Cell* **149**, 708–721 (2012).
45. Iaccarino, H. F. et al. Gamma frequency entrainment attenuates amyloid load and modifies microglia. *Nature* **540**, 230–235 (2016).
46. Martorell, A. J. et al. Multi-sensory gamma stimulation ameliorates Alzheimer's-associated pathology and improves cognition. *Cell* **177**, 256–271 (2019).
47. Ohmuro, N. et al. The relationship between cognitive insight and cognitive performance among individuals with at-risk mental state for developing psychosis. *Schizophr. Res.* **192**, 281–286 (2018).
48. Lappin, J. M. et al. Insight in individuals with an at risk mental state. *Schizophr. Res.* **90**, 238–244 (2007).

Methods

Further information and requests for resources and reagents should be directed to and will be fulfilled by Vikaas Sohal (vikaas.sohal@ucsf.edu).

Mice. All animal care, procedures and experiments were conducted in accordance with National Institues of Health guidelines and approved by the Administrative Panels on Laboratory Animal Care at the University of California, San Francisco. Mice were group housed (2–5 siblings) in a temperature-controlled environment (22–24 °C), had ad libitum access to food and water and were reared in normal lighting conditions (12-h light/dark cycle) until rule shift experiments began. *Dlx5/6* mice[14,49] were backcrossed to C57Bl/6 mice for at least six generations and then crossed to the Cre driver lines: *PV-Cre* (The Jackson Laboratory), *Sst-Cre* (The Jackson Laboratory) and Ai14 (The Jackson Laboratory). Both male and female adult mice (10–20 weeks old at the time of the experiment) were used in the behavioral experiments. All experiments were done using *Dlx5/6*$^{+/-}$ mice and their age-matched *Dlx5/6*$^{+/+}$ littermates (crossed to *PV-Cre*, *Sst-Cre* and/or Ai14 lines). All experiments that contained different groups of mice—for example, *Dlx5/6*$^{+/+}$ and *Dlx5/6*$^{+/-}$ mice or ChR2-expressing and eYFP-expressing mice—were performed blinded to genotype and/or virus injected. This was the case for all experiments except for the experiments shown in Fig. 3 (in which all mice were *Dlx5/6*$^{+/+}$*;PV-Cre* Ai14) and Fig. 6a–c (in which all mice were *Dlx5/6*$^{+/-}$*;PV-Cre* and expressed ChR2). All subjects were randomly assigned to different experimental conditions used in this study. Animals included in each experiment are described in Supplementary Table 1.

When we initially began experiments, we were uncertain whether the Ai14-driven tdTomato fluorescence would be similar in magnitude to the mNeon fluorescence, so, as noted below, we also injected a subset of animals with virus to drive additional tdTomato expression. It turned out that the reference fluorophore signals were similar in magnitude and adequate in both cases, so, in later cohorts, we no longer injected additional tdTomato virus.

Cloning of viral constructs. To produce AAV5-I12b-BG-DIO-eYFP (2.1×10^{13} vg ml^{-1}), we introduced MluI- and BamHI-compatible sticky ends to the DlxI12b-BG sequence with PCR. The pAAV-EF1α-DIO-eYFP (Addgene) was then cut with MluI and BamHI and ligated to the PCR insert to exchange the EF1α promoter for DlxI12b-BG. Virus was packaged by Virovek with serotype AAV5.

To produce AAV1-CAG-DIO-Ace2N-4AA-mNeon (2.23×10^{13} vg ml^{-1}), we received pAAV-CAG-DIO-Ace2N-4AA-mNeon from Mark J. Schnitzer (Stanford University). Virus was packaged by Virovek with serotype AAV1.

Surgery. Male and female mice were anaesthetized using isoflurane (2.5% induction, 1.2–1.5% maintenance, in 95% oxygen) and placed in a stereotaxic frame (David Kopf Instruments). Body temperature was maintained using a heating pad. An incision was made to expose the skull for stereotaxic alignment using bregma and lambda as vertical references. The scalp and periosteum were removed from the dorsal surface of the skull and scored with a scalpel to improve implant adhesion. Viruses were infused at 100–150 nl per min through a 35-gauge, beveled injection needle (World Precision Instruments) using a microsyringe pump (World Precision Instruments, UMP3 UltraMicroPump). After infusion, the needle was kept at the injection site for 5–10 min and then slowly withdrawn. After surgery, mice were allowed to recover until ambulatory on a heated pad and then returned to their homecage.

For behavioral experiments using Cre-dependent optogenetic opsins, mice were injected bilaterally in the mPFC, near the border between the prelimbic and infralimbic cortices (1.7 anterior–posterior (AP), ±0.3 mediolateral (ML) and −2.75 dorsoventral (DV) mm relative to bregma) with 1 µl of AAV5-EF1α-DIO-ChR2-eYFP (7.4×10^{12} vg ml^{-1}; UNC Virus Core) or 1 µl of AAV5-I12b-BG-DIO-ChR2-eYFP or 1 µl of AAV5-EF1α-DIO-eYFP (6×10^{12} vg ml^{-1}; UNC Virus Core) per hemisphere, to selectively target neurons expressing Cre. *Dlx5/6, Sst-Cre* mice were injected bilaterally in the mPFC (1.7 AP, ±0.3 ML and −2.75 DV) with 1 µl of AAV5- EF1α-DIO-ChR2-eYFP or 1 µl of AAV5-EF1α-DIO-eYFP per hemisphere. After injection of virus, a 200/240-µm (core/outer) diameter, NA = 0.22, dual fiber-optic cannula (Doric Lenses, DFC_200/240-0.22_2.3mm_GS0.7_FLT) was slowly inserted into the mPFC until the tip of the fiber reached a DV depth of −2.25. Implants were affixed onto the skull using Metabond Quick Adhesive Cement (Parkell). We waited at least 5 weeks after injection before behavioral experiments to allow for virus expression. For experiments using LFP recordings, standard-tip 0.4-MΩ-impedance tungsten microelectrodes (Microprobes) were used. The coordinates were adjusted to accommodate experiments whereby LFP electrodes were affixed to the fiber implant and protruded 200–300 µm beyond the fiber tip. A common reference screw was implanted into the cerebellum: −5 (AP), 0 (ML), and a ground screw was implanted at −5 (AP), −3 (ML). After affixing the electrodes in place using Metabond (Parkell), connections were made to the headstage of a multichannel recording system (Pinnacle Technology).

For behavioral experiments used in photometry experiments, mice were injected unilaterally at four depths (DV: −2.75, −2.5, −2.25 and −2.0) at the following AP/ML for mPFC: 1.7 AP, 0.3 ML with 4 ×0.2 µl of AAV2/1-Syn-FLEX–GCaMP6f-WPRE-SV40 (2.28×10^{13} vg ml^{-1}; UPenn Virus Core). After injection of virus, a 400/430-µm (core/outer) diameter, NA = 0.48, multimode fiber implant (Doric Lenses, MFC_400/430-0.48_2.8mm_ZF2.5_FLT) was slowly inserted into the mPFC until the tip of the fiber reached a DV depth of −2.25. We waited at least 4 weeks after injection before behavioral experiments to allow for virus expression.

For behavioral experiments used in dual-site TEMPO experiments, mice were injected bilaterally at three depths (DV: −2.5, −2.25 and −2.0) at the following AP/ML for mPFC: 1.7 AP, ±0.3 ML with 3 ×0.2 µL of AAV1-CAG-DIO-Ace2N-4AA-mNeon (Virovek) or with the addition of 0.1 µl per depth of AAV2-Syn-tdTomato (1.23×10^{12} vg ml^{-1}; SignaGen Laboratories). After injection of virus, a 400/430-µm (core/outer) diameter, NA = 0.48, multimode fiber implant (Doric Lenses, MFC_400/430-0.48_2.8mm_ZF1.25_FLT) was slowly inserted into the mPFC at a 12-degree angle using the following coordinates: 1.7 (AP), ±0.76 (ML), −2.13 (DV). We waited at least 5 weeks after injection before behavioral experiments to allow for virus expression.

For in vivo awake head-fixed recordings, *PV-Cre* mice were injected unilaterally in the mPFC, near the border between the prelimbic and infralimbic cortices (1.7 AP, +0.3 ML and −2.75 DV mm relative to bregma) with 1 µl of AAV5-EF1α-DIO-ChR2-eYFP (7.4×10^{12} vg ml^{-1}; UNC Virus Core), to selectively target neurons expressing Cre. At least 3 weeks later, mice were implanted with a circular head bar at least 2 weeks before the day of the recording. The animals were anesthetized with 2% isoflurane, the scalp was removed and the skull was disinfected with alcohol and povidone iodine and scored with a bone scraper. The edge of the skin was glued to the skull, and the metal head bar was sterilized and mounted using the dental cement RelyX Unicem 2 Automix (3M ESPE). The head bar was stereotactically mounted with the help of an inclinometer (Digi-Key Electronics, 551-1002-1-ND). The inclinometer was instrumental in calibrating the angle of the two axes of the head bar in relation to the sagittal and medio–lateral axes of the head. After the bar implantation, black dental cement was used to build a recording well surrounding the recording site. The surface of the skull above the right PFC was not covered with dental cement but coated with a thin layer of transparent cyanoacrylate glue. Animals were injected subcutaneously with 0.1 mg kg^{-1} buprenorphine and checked daily after the head bar surgery. For at least 4 d before recording, mice were habituated to head fixation within the recording setup.

On the day before recording, mice were anesthetized with 2% isoflurane, and the layer of cyanoacrylate glue covering the recording sites was drilled off. The dura was not removed, and the exposed brain was kept moist with artificial cerebrospinal fluid (140 mM NaCl, 5 mM KCl, 10 mM D-glucose, 10 mM HEPES, 2 mM $CaCl_2$, 2 mM $MgSO_4$, pH 7.4). Three of four animals were recorded a second time at least 8 h after the first recording. The electrode was moved from 0.3 ML, 1.5 AP to 0.3 ML, 1.7 AP, so, more anterior. The depth of the recorded units varied between 1.78 and 2.42 mm from pia.

Rule shift task. This cognitive flexibility task was described previously[14]. Briefly, mice are singly housed and habituated to a reverse light/dark cycle, and food intake is restricted until the mouse is 80–85% of its ad libitum feeding weight. At the start of each trial, the mouse was placed in its home cage to explore two bowls, each containing one odor and one digging medium, until it dug in one bowl, signifying a choice. As soon as a mouse began to dig in the incorrect bowl, the other bowl was removed, so there was no opportunity for 'bowl switching.' (Digging is defined as the sustained displacement of the media within a bowl). The bait was a piece of a peanut butter chip (approximately 5–10 mg in weight), and the cues, either olfactory (odor) or somatosensory and visual (texture of the digging medium that hides the bait), were altered and counterbalanced. All cues were presented in small animal food bowls (All Living Things Nibble Bowls, PetSmart) that were identical in color and size. Digging media were mixed with the odor (0.01% by volume) and peanut butter chip powder (0.1% by volume). All odors were ground dried spices (McCormick garlic and coriander) and unscented digging media (Mosser Lee White Sand Soil Cover, Integrity Clumping Clay Cat Litter).

After mice reached their target weight, they underwent 1 d of habituation. On this day, mice were given ten consecutive trials with the baited food bowl to ascertain that they could reliably dig and that only one bowl contained food reward. All mice were able to dig for the reward. Mice did not undergo any other specific training before being tested on the task. Then, on days 1 and 2 (and, in some cases, on additional days as well), mice performed the task (this was the testing done for experiments). After the task was done for the day, the bowls were filled with different odor–medium combinations, and food was evenly distributed among these bowls and given to the mouse so that the mouse would disregard any associations made earlier in the day.

Mice were tested through a series of trials. The determination of which odor and medium to pair and which side (left or right) contained the baited bowl was randomized (subject to the requirement that the same combination of pairing and side did not repeat on more than three consecutive trials) using http://random.org. On each trial, although the particular odor–medium combination present in each of the two bowls might have changed, the particular stimulus (for example, a particular odor or medium) that signaled the presence of food reward remained constant over each portion of the task (initial association and rule shift). If the initial association paired a specific odor with food reward, then the digging medium would be considered the irrelevant dimension. The mouse was considered

to have learned the initial association between stimulus and reward if it made eight correct choices during ten consecutive trials. Each portion of the task ended when the mouse met this criterion. After the initial association, the rule shift portion of the task began, and the particular stimulus associated with reward underwent an extra-dimensional shift. For example, if an odor had been associated with reward during the initial association, then a digging medium was associated with reward during the rule shift portion of the task. The mouse was considered to have learned this extra-dimensional rule shift if it made eight correct choices during ten consecutive trials. When a mouse made a correct choice on a trial, it was allowed to consume the food reward before the next trial. After correct trials, the mouse was transferred from the home cage to a holding cage for about 10 s while the new bowls were set up (ITI). After making an error on a trial, a mouse was transferred to the holding cage for about 2 min (ITI). All animals performed the initial association in a similar number of trials (average, 10–15 trials). We were blinded to genotype and/or virus injected. Videos were manually scored with a temporal resolution of 1 s.

For analyses (described below), we chose the onset of digging as the time of a decision for two reasons. First, as noted above, once a mouse began to dig in the incorrect bowl, the other (correct) bowl was removed. Second, only upon the commencement of digging could a mouse determine whether reward was present in the chosen bowl and obtain feedback about whether it had made a correct choice. We regarded the end of digging (that is, the beginning of a sustained period of not digging) as the end of the trial, because immediately after this timepoint, the mouse was removed from the test cage and placed in a holding cage for the ITI.

Rule reversal task. This cognitive flexibility task was described previously[14]. Similarly to the mechanics of the rule shift task described above, after the initial association, the rule reversal portion of the task began, and the particular stimulus associated with reward underwent an intra-dimensional shift. For example, if an odor had been associated with reward during the initial association, then the previously unrewarded odor was associated with reward during the rule reversal portion of the task. The mouse was considered to have learned this intra-dimensional rule reversal if it made eight correct choices during ten consecutive trials.

Mice that were involved in both the rule shift and rule reversal tasks were randomly assigned the order of tasks over the course of 2 d.

In vivo optogenetic stimulation. In-phase ChR2 stimulation: a 473-nm blue laser (OEM Laser Systems) was coupled to the dual fiber-optic cannula (Doric Lenses) through a 200-µm-diameter dual fiber-optic patchcord with guiding socket (Doric Lenses) and one ×2 intensity division fiber-optic rotary joint (Doric Lenses) and adjusted such that the final light power was ~0.5 mW total, summed across both fibers and averaged over light pulses and the intervening periods. A function generator (Agilent 33500B Series Waveform Generator) connected to the laser generated a 40-Hz train of 5-ms pulses.

Out-of-phase ChR2 stimulation: the stereotaxically implanted dual fiber-optic cannula was coupled to two separate 473-nm blue lasers via a dual fiber-optic patch cord with fully separated optical paths that were each connected to separate fiber-optic rotary joints. Again, light power was adjusted such that the final output was ~0.5 mW across both fibers. Different function generators connected to each laser to generate out-of-phase stimulation. For the experiments shown in Fig. 4d–e and Fig. 6d–f, these two function generators were not connected in any way, except that we verified (by eye) that the light pulses were delivered at non-overlapping times, producing phase differences between 72 and 288 degrees. For the experiments shown in Fig. 4a–c and Fig. 4f–h, one function generator was triggered at the time when the other function generator switched off, so the phase difference was exactly 72 degrees. Stimulation was generated using either a 20-Hz train of 10-ms pulses or a 40-Hz train of 5-ms pulses.

For all experiments in which we delivered optogenetic stimulation to behaving mice, light stimulation began once mice reached the 80% criterion during the initial association portion of the task. Mice then performed three additional initial association trials with the light stimulation before the rule shift portion of the task began. The light stimulation did not alter the performance or behavior of the mice during these three extra trials of the initial association. Experiments were performed blinded to genotype and/or virus injected.

Drug administration. Clonazepam at indicated concentrations (0.0625 mg kg^{-1}, Sigma) was diluted in the vehicle solution (phosphate-buffered saline (PBS) with 0.5% methylcellulose) and then injected (intraperitoneally) in a volume of 0.01 ml kg^{-1} 30 min before behavioral testing.

Fiber photometry design and recording. The photometry apparatus and analysis was as described previously[26], with some modifications described below.

A fiber-optic stub (400-µm core, NA = 0.48, low-autofluorescence fiber; Doric Lenses, MFC_400/430-0.48_2.3mm_ZF2.5_FLT) was stereotaxically implanted in the mPFC. A single fiber was used to both deliver excitation light and collect emitted fluorescence from the recording site. A matching fiber-optic patch cord (Doric Lenses, MFP_400/430/1100-0.48_2m_FC-ZF2.5) provided a light path between the animal and a miniature, permanently aligned optical bench, or 'mini cube' (Doric Lenses, FMC2_AF405-GCaMP_FC). Two excitation LEDs (470-nm 'blue' and 405-nm 'violet', Thorlabs, M470F1 and M405FP1) were connected to the 'mini cube' by a patch cord (200-µm core, NA = 0.39, Doric Lenses) and controlled by an LED driver (Thorlabs, DC4104) and connected to an RX-8 real-time processor (Tucker-Davis Technologies). Excitation light was delivered at 470 nm to stimulate GCaMP6f fluorescence in a Ca^{2+}-dependent manner and at 405 nm, an excitation isosbestic wavelength for GCaMP6f, to perform ratiometric measurements of GCaMP6f activity, correcting for bleaching and artifactual signal fluctuations. Blue excitation was sinusoidally modulated at 210 Hz, and violet excitation was modulated at 330 Hz. The GCaMP6f emission signal was collected through a patchcord (Doric Lenses, MFP_600/630/LWMJ-0.48_0.5m_FC-FC) and focused onto a femtowatt photoreceiver (Newport, 2151) with a lensed, permanently aligned FC coupler (Doric Lenses). Each of the two modulated signals generated by the two LEDs was independently recovered using standard synchronous demodulation techniques implemented on the RX-8 real-time processor. The commercial software Synapse (Tucker-Davis Technologies) running on a PC was used to control the signal processor, write data streams to disk and record synchronized video from a generic infrared USB webcam (Ailipu Technology, ELP-USB100W05MT-DL36). Files were then exported for analysis to MATLAB (MathWorks).

For every experiment, the far end of the patch cord and the 2.5-mm-diameter zirconia optical implant ferrule were cleaned with isopropanol before each recording and then securely attached via a zirconia sleeve.

LFP recording. Data were recorded at 1 kHz, and analog signals were digitized by a multichannel real-time signal processor (Tucker-Davis Technologies, RX-8). The commercial software Synapse (Tucker-Davis Technologies) running on a PC was used to control the signal processor, write data streams to disk and record synchronized video from a generic infrared USB webcam (Ailipu Technology, ELP-USB100W05MT-DL36). Channels shared a common reference (cerebellum). In one experiment, LFPs were recorded in freely moving mice in their home cage, either when optogenetic stimulation was absent (baseline period) or during delivery of optogenetic stimulation to prefrontal PV interneurons. Patterns of optogenetic stimulation and methods for expressing ChR2 in PV interneurons were the same as in behavioral experiments (see above). In another experiment, we recorded LFPs from the left and right mPFC while mice performed the rule shift task.

In vivo awake head-fixed recordings. Extracellular recordings from the PFC were performed using opto-silicon probes: ASSY-37 H4 (acute 32 channel H4 opto-electrode, one shank, 9-mm length). The recording electrodes were controlled with Luigs & Neumann micromanipulators and stained with DiI lipophilic dyes (Life Technologies) for post hoc identification of the electrode track. We recorded the signals at 30 kHz using an Intan system (RHD2000 USB Interface Board, Intan Technologies). Automated spike sorting was then carried out using Kilosort (https://github.com/cortex-lab/Kilosort) by manual curation of the units using Phy (https://phy.readthedocs.io/en/latest/). Light power was adjusted such that the final output was ~0.25 mW when delivering 40-Hz, 5-ms pulses for DIO-ChR2 activation. Units were identified and all following analysis was carried out using routines written in Matlab. We excluded units with refractory period violations greater than 1%. Neurons were considered as putative PV neurons when their firing increased and was significantly different from the baseline activity ($P < 0.01$) during 5-ms blue light pulse activation at 1 Hz. Regular-spiking and fast-spiking neurons were identified based on spike shape. The average peristimulus time histogram of PV cell responses was calculated from minute 1 through 4 of the 40-Hz, 5-ms ChR2 activation.

Dual-site voltage–sensor photometry (TEMPO). High-bandwidth, time-varying bulk fluorescence signals were measured at each recording site using the TEMPO technique described in ref. [28], with some modifications as described below.

Optical apparatus. A fiber-optic stub (400-µm core, NA = 0.48, low-autofluorescence fiber; Doric Lenses, MFC_400/430-0.48_2.8mm_ZF1.25_FLT) was stereotaxically implanted in each targeted brain region. A matching fiber-optic patch cord (Doric Lenses, MFP_400/430/1100-0.48_2m_FC-ZF1.25) provided a light path between the animal and a miniature, permanently aligned optical bench, or 'mini-cube' (Doric Lenses, FMC5_E1(460-490)_F1(500-540)_E2(555-570)_F2(580-680)_S). A single fiber was used to both deliver excitation light to and collect emitted fluorescence from each recording site. The far end of the patch cord and each 1.25-mm-diameter zirconia optical implant ferrule were cleaned with isopropanol before each recording and then securely attached via a zirconia sleeve.

The mini-cube optics allow for the simultaneous monitoring of two spectrally separated fluorophores, with dichroic mirrors and cleanup filters chosen to match the excitation and emission spectra of the voltage sensor and reference fluorophores in use ('mNeon' voltage sensor channel: excitation, 460–490 nm, emission, 500-540 nm; 'Red' control fluorophore: excitation, 555–570 nm, emission, 580–680 nm). The mini-cube optics were sealed and permanently aligned, and all five ports (sample to animal, two excitation lines and two emission lines) were provided with matched coupling optics and FC connectors to allow for a modular system design.

Excitation light for each of the two color channels was provided by a fiber-coupled LED (center wavelengths, 490 nm and 565 nm, Thorlabs, M490F3 and M565F3) connected to the mini-cube by a patch cord (200 µm, NA = 0.39; Thorlabs, M75L01). Using a smaller diameter for this patch cord than for the patch cord from the cube to the animal is critical to reduce the excitation spot size on the output fiber face and thus avoid cladding autofluorescence. LEDs were controlled by a four-channel, 10-kHz-bandwidth current source (Thorlabs, DC4104). LED current was adjusted to give a final light power at the animal (averaged during modulation, see below) of approximately 200 µW for the mNeon channel (460–490-nm excitation) and 100 µW for the Red channel (555–570-nm excitation).

Each of the two emission ports on the mini-cube was connected to an adjustable-gain photoreceiver (Femto, OE-200-Si-FC; bandwidth set to 7 kHz, AC coupled, 'Low' gain of ~5×10^7 V/W) using a large-core high-NA fiber to maximize throughput (600-µm core, NA = 0.48 (Doric lenses, MFP_600/630/LWMJ-0.48_0.5m_FC-FC).

Note that, for dual-site recordings, two completely independent optical setups were employed, with separate implants, patch cords, mini-cubes, LEDs, photoreceivers and lock-in amplifiers.

Modulation and lock-in detection. At each recording site, each of the two LEDs was sinusoidally modulated at a distinct carrier frequency to reduce crosstalk due to overlap in fluorophore spectra. The corresponding photoreceiver outputs were then demodulated using lock-in amplification techniques. A single instrument (Stanford Research Systems, SR860) was used to generate the modulation waveform for each LED and to demodulate the photoreceiver output at the carrier frequency. To further reduce crosstalk between recording sites, distinct carrier frequencies were used across at each site (mNeon site 1: 2 kHz; mNeon site 2: 2.5 kHz; Red site 1: 3.5 kHz; Red site 2: 4 kHz). Low-pass filters on the lock-in amplifiers were selected to reject noise above the frequencies under study (cascade of four Gaussian FIR filters with 84-Hz equivalent noise bandwidth; final attenuation of signals were approximately −1 dB (89% of original magnitude) at 20 Hz, −3 dB (71% of original magnitude) at 40 Hz and −6 dB (50% of original magnitude) at 60 Hz).

TEMPO recording. Analog signals were digitized by a multichannel real-time signal processor (Tucker-Davis Technologies, RX-8). The commercial software Synapse (Tucker-Davis Technologies) running on a PC was used to control the signal processor, write data streams to disk and record synchronized video from a generic infrared USB webcam (Ailipu Technology, ELP-USB100W05MT-DL36). Lock-in amplifier outputs were digitized at 3 kHz.

Histology and imaging. All mice used for behavioral and imaging experiments were anesthetized with Euthasol and transcardially perfused with 30 ml of ice-cold 0.01 M PBS followed by 30 ml of ice-cold 4% paraformaldehyde (PFA) in PBS. Brains were extracted and stored in 4% PFA for 24 h at 4 °C before being stored in PBS. Next, 50-µm and 70-µm slices were obtained on a Leica VT100S and mounted on slides. All imaging was performed on an Olympus MVX10, Nikon Eclipse 90i, Zeiss LSM510 or Zeiss Axioskop 2. Representative images for all figures are enlarged in Supplementary Fig. 1. We verified that all mice had virus-driven expression and optical fibers located in the mPFC.

Fiber photometry analysis. For calculating peak GCaMP6f signals during activity time locked to task-related events: at the beginning of each trial, at the time of each decision (indicated by the mouse beginning to dig in one bowl) and at the beginning and end of each ITI, a least-squares linear fit was applied to the 405-nm control signal to align it to the 470-nm signal. The $\Delta F/F$ time series was then calculated for each behavioral session as: ((470-nm signal − fitted 405-nm signal) / fitted 405-nm signal). For points of interest (for example, time of decision), peak $\Delta F/F$ was calculated as the most extreme $\Delta F/F$ value at time 0–4 s (positive or negative) for *PV-Cre* experiments and at time 4–8 s (positive or negative) for *Sst-Cre* experiments. Experiments were performed, scored and analyzed blinded to genotype.

LFP analysis. To analyze changes in power in our LFP data, we computed spectrograms from completely non-overlapping time windows and compared unnormalized power (measured in log units) during 40-Hz optical stimulation to the power during the baseline period.

To quantify zero-phase-lag synchrony between LFPs recorded from the left and right mPFC, we calculated the square of the real part of the wavelet cross spectrum, obtained from the *wcoherence* function in Matlab.

TEMPO analysis. Analysis of TEMPO data was facilitated using the signal processing toolbox and MATLAB, using the following functions: fir1, filtfilt and regress. All four signals during the entire time series of the experiment (left mNeon, left tdTomato, right mNeon and right tdTomato) were first filtered around a frequency of interest. To quantify zero-phase-lag cross-hemispheric synchronization between left and right mNeon signals, we performed a linear regression analysis to predict the right mNeon signal using the following inputs: left mNeon signal, left tdTomato signal and right tdTomato signal. The goodness of fit was compared to how well the regression works if the left mNeon signal is shuffled—that is, if we use a randomly chosen segment of the original left mNeon signal, instead of the segment recorded at the same time as the right mNeon signal. R^2 values were calculated as a function of time using 1-s segments and compared to the 99th percentile of the distribution of R^2 values obtained from 100 fits to randomly shuffled data. The fraction of timepoints at which the R^2 obtained from actual data exceeded the 99th percentile of the R^2 values obtained from shuffled data was used to measure zero-phase-lag synchronization between the left and right mNeon signals.

We performed this analysis at the time of the decision (for example, immediately after the beginning of digging in one bowl until the end of digging) and smoothed measurements over a 5-min time window after the time point of interest. We also confirmed that our TEMPO findings did not change when we did not smooth over any window but instead simply averaged R^2 values from the start of the trial until the end of the subsequent ITI. To measure 90-degree out-of-phase synchronization, the filtered left mNeon signal was simply advanced 90 degrees relative to the right mNeon signal, before performing the analysis described above. Experiments were performed, scored and analyzed blinded to genotype. Note: mice that did not make both correct and incorrect decisions in the first five trials of a task could not be used for analyses that compared activity on correct versus incorrect decisions.

Data analyses and statistics. Statistical analyses were performed using Prism 7 (GraphPad) and detailed in the corresponding figure legends. Quantitative data are expressed as the mean, and error bars or shaded areas represent the s.e.m. Group comparisons were made using one-way repeated-measures or two-way ANOVA followed by Tukey's or Bonferroni post hoc tests to control for multiple comparisons, respectively. Paired and unpaired two-tailed Student's *t*-tests were used to make single-variable comparisons or with Welch's correction for unequal variance. Similarity of variance between groups was confirmed by the *F* test. Measurements were taken from distinct samples. $P = *, < 0.05$; **, < 0.01; ***, < 0.001; ****, < 0.0001. Comparisons with no asterisk had $P > 0.05$ and were considered not significant. No statistical methods were used to predetermine sample sizes, but our sample size choice was based on previous studies[14] and are consistent with those generally employed in the field. Data distribution was assumed to be normal, but this was not formally tested.

Reporting Summary. Further information on research design is available in the Life Sciences Reporting Summary linked to this article.

Data availability

The data that support the findings of this study are available from the corresponding author upon reasonable request.

Code availability

Scripts used to analyze dual-site TEMPO data are deposited at https://github.com/sohallab/dual-site-TEMPO.

References

49. Wang, Y., et al. Dlx5 and Dlx6 regulate the development of parvalbumin-expressing cortical interneurons. *J. Neurosci.* **30**, 5334–5345 (2010).

Acknowledgements

This work was supported by the National Institute of Mental Health (R01MH106507 to V.S.S. and K99MH108720 to K.K.A.C.), the Brain and Behavior Foundation (NARSAD Young Investigator Award to K.K.A.C.), the McKnight Foundation (Memory and Cognitive Disorders award to V.S.S.) and the Brain Research Foundation (Scientific Innovations Award to V.S.S.). We appreciate helpful feedback on earlier versions of this manuscript from L. Frank and M. Scanziani.

Author contributions

K.K.A.C. and V.S.S. designed experiments and wrote the manuscript. K.K.A.C. performed all the experiments, except that G.B. performed and analyzed the opto-tagging experiment. T.J.D. and K.K.A.C. set up the LED photometry rig and the dual-site TEMPO rig. K.K.A.C. generated AAV5-I12b-BG-DIO-eYFP. J.D.M. and M.J.S. provided guidance, advice and feedback on the acquisition and analysis of TEMPO data. K.K.A.C. and V.S.S. analyzed the data.

Competing interests

The authors declare no competing interests.

Additional information

Extended data is available for this paper at https://doi.org/10.1038/s41593-020-0647-1.

Supplementary information is available for this paper at https://doi.org/10.1038/s41593-020-0647-1.

Correspondence and requests for materials should be addressed to V.S.S.

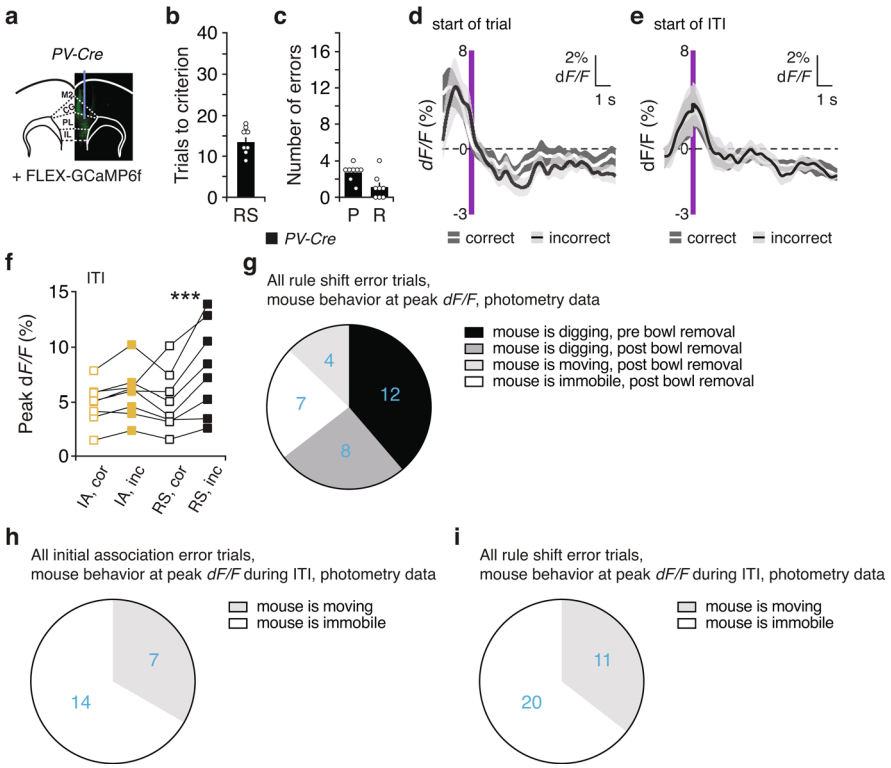

Extended Data Fig. 1 | Photometry signals from PV interneurons and behavior during rule shifts in mice used for photometry experiments. a, *PV-Cre* mice had a unilateral FLEX-GCaMP6f injection and fiber-optic implant in mPFC for photometry (scale bar, 100 μm). **b**, Rule-shift (RS) performance of *PV-Cre* mice ($n = 8$) used for photometry experiments. **c**, Numbers of perseverative (P) or random (R) errors during the rule shift of *PV-Cre* mice ($n = 8$). **d**, Averaged PV interneuron photometry signal (*dF/F*), aligned to the start of each trial, for correct (white line) vs. incorrect trials (black line; $n = 8$). **e**, Averaged PV interneuron photometry signal (*dF/F*), aligned to the start of the intertrial interval (ITI), for correct (white line) vs. incorrect trials (black line; $n = 8$) for the first ten seconds of ITIs. **f**, Peak *dF/F* during the entire intertrial interval (ITI), usually lasting around two minutes. Signals are significantly higher on incorrect rule shift trials than correct rule shift trials ($n = 8$ mice; two-way ANOVA; main effect of outcome: $F_{1,14} = 26.53$, $^{***}P = 0.0001$; task X outcome interaction: $F_{1,14} = 7.47$, $^{*}P = 0.016$; RS correct versus incorrect, post hoc $t_{(14)} = 5.58$, $^{***}P = 0.0001$; IA correct versus incorrect, post hoc $t_{(14)} = 1.71$, $P = 0.22$). **g**, Mouse behavior scored at the time of the peak *dF/F* signal during rule shift error trials ($n = 31$ error trials of 8 mice). **h**, Mouse behavior scored at the time of the peak *dF/F* signal during initial association error ITI ($n = 21$ error ITIs of 8 mice). **i**, Mouse behavior scored at the time of the peak *dF/F* signal during rule shift error ITI ($n = 31$ error ITIs of 8 mice). Data are shown as means (**b**, **c**); error bars (**b**, **c**) and shading (**d**, **e**) denote s.e.m. Two-way ANOVA followed by Bonferroni post hoc comparisons were used. Comparisons were not significant unless otherwise noted.

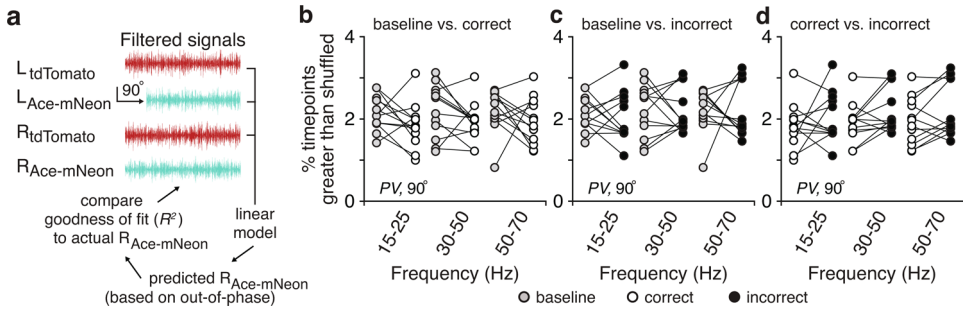

Extended Data Fig. 2 | Cross-hemispheric synchrony of PV interneurons at non-zero phase lag. a, Schematic: analysis to measure out-of-phase synchrony. In this case, one Ace-mNeon is signal is shifted 90 degrees out-of-phase relative to the other signals, before following the procedure outlined in Fig. 2e. **b**–**d**, Out-of-phase 30-50 Hz synchrony ($n = 12$ mice) did not differ between the baseline period and RS correct trials (two-way ANOVA; frequency X condition interaction: $F_{2,33} = 0.16$, $P = 0.86$; post hoc $t_{(33)} = 1.35$, $P = 0.56$), baseline period and RS incorrect trials (two-way ANOVA; frequency X condition interaction: $F_{2,33} = 0.06$, $P = 0.94$; post hoc $t_{(33)} = 0.05$, $P > 0.99$), or correct and incorrect trials (two-way ANOVA; frequency X condition interaction: $F_{2,33} = 0.05$, $P = 0.95$; post hoc $t_{(33)} = 1.53$, $P = 0.41$). Two-way ANOVA followed by Bonferroni post hoc comparisons were used. Comparisons were not significant.

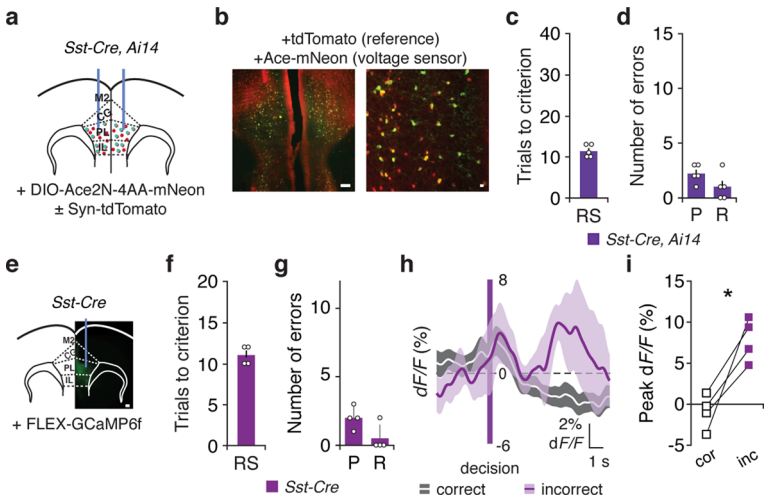

Extended Data Fig. 3 | Learning during rule shifts in mice used for TEMPO measurements from Sst interneurons, and photometry signals from Sst interneurons during rule shifts. a, *Sst-Cre* Ai14 mice had bilateral AAV-DIO-Ace2N-4AA-mNeon ± AAV-Syn-tdTomato injections and fiber-optic implants in mPFC. **b**, Representative images of tdTomato (red) and Ace-mNeon (green) fluorescence in a coronal section of mPFC (left), alongside a high power image (right). Scale bars: 100 μm and 25 μm, respectively. **c**, Rule-shift (RS) performance of *Sst-Cre* Ai14 mice ($n = 5$) used for dual-site TEMPO imaging. **d**, Number of perseverative (P) and random (R) errors during the rule shift of *Sst-Cre* Ai14 mice ($n = 5$). **e**, *Sst-Cre* mice had a unilateral FLEX-GCaMP6f injection and fiber-optic implant in mPFC for photometry (scale bar, 100 μm). **f**, Rule-shift (RS) performance of *Sst-Cre* mice ($n = 4$) used for photometry experiments. **g**, Numbers of perseverative (P) or random (R) errors during the rule shift *Sst-Cre* mice ($n = 4$). **h**, Averaged Sst interneuron photometry signal (*dF/F*), aligned to the time of dig, which indicates a decision, for correct (white line) vs. incorrect trials (purple line; $n = 4$). **i**, Peak *dF/F* during the 4-8 sec following the decision (this was the time at which peak Sst activity occurred). Sst interneuron photometry signals are significantly higher on incorrect than correct trials ($n = 4$ mice; two-tailed, paired *t*-test; $t_{(3)} = 4.65$, $^*P = 0.02$). Data are shown as means (**c**, **d**, **f**, **g**, **h**); error bars (**c**, **d**, **f**, **g**) and shading (**h**) denote s.e.m.

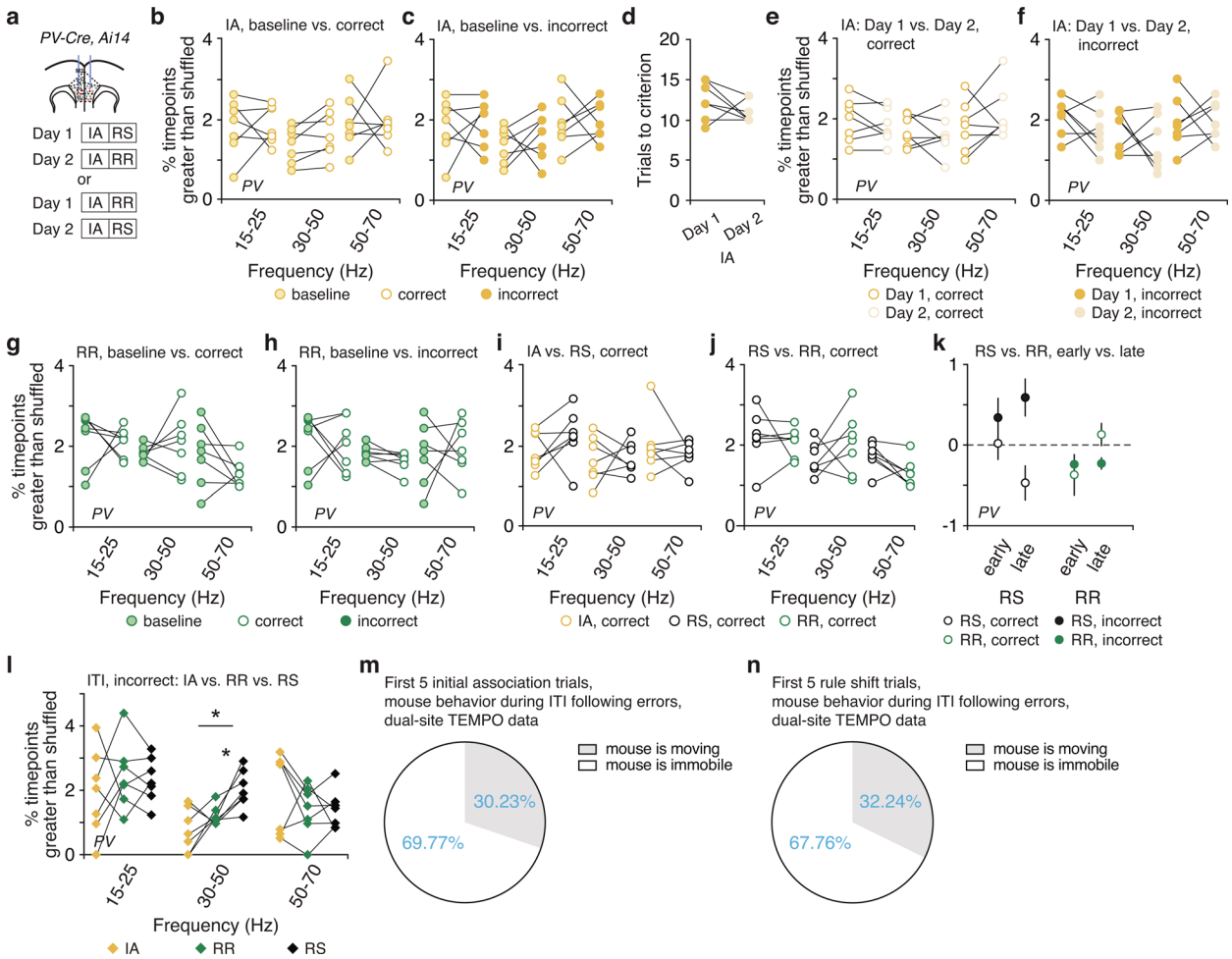

Extended Data Fig. 4 | Cross-hemispheric synchrony between prefrontal PV interneurons for various frequency bands and types of trials. a, *PV-Cre* Ai14 mice had bilateral AAV-DIO-Ace2N-4AA-mNeon ± AAV-Syn-tdTomato injections and fiber-optic implants in mPFC. Experimental design: Day 1: Initial association (IA) followed by rule shift (RS) or rule reversal (RR); Day 2: IA followed by the rule change (RS or RR) that was not performed on Day 1. **b**, During learning of the IA that preceded the RS, synchrony was not different after correct decisions vs. during the baseline period ($n=7$ mice; two-way ANOVA; main effect of condition: $F_{1,18}=0.51$, $P=0.48$; frequency X condition interaction: $F_{2,18}=0.20$, $P=0.82$). **c**, During learning of this IA, synchrony was not different after incorrect decisions vs. during the baseline period ($n=7$ mice; two-way ANOVA; main effect of condition: $F_{1,18}=0.39$, $P=0.54$; frequency X condition interaction: $F_{2,18}=0.07$, $P=0.94$). **d**, IA performance was not different across days ($n=7$ mice; two-tailed, paired *t*-test; $t_{(6)}=1.29$, $P=0.25$). **e**, There was no difference in synchrony after correct trials during learning of the IA on Day 1 vs. 2 ($n=7$ mice; two-way ANOVA; main effect of day: $F_{1,18}=0.02$, $P=0.89$; frequency X condition interaction: $F_{2,18}=1.48$, $P=0.26$). **f**, There was no difference in synchrony after incorrect trials during learning of the IA on Day 1 vs. 2 ($n=7$ mice; two-way ANOVA; main effect of day: $F_{1,18}=3.05$, $P=0.10$; frequency X condition interaction: $F_{2,18}=0.03$, $P=0.97$). **g**, During the RR, synchrony was not different after correct decisions vs. during the baseline period ($n=7$ mice; two-way ANOVA; main effect of condition: $F_{1,18}=0.28$, $P=0.60$; frequency X condition interaction: $F_{2,18}=1.24$, $P=0.31$). **h**, During the RR, synchrony was not different after incorrect decisions vs. the baseline period ($n=7$ mice; two-way ANOVA; main effect of condition: $F_{1,18}=0.09$, $P=0.77$; frequency X condition interaction: $F_{2,18}=0.30$, $P=0.74$). **i**, Synchrony after correct decisions did not differ between the IA vs. RS ($n=7$ mice; two-way ANOVA; main effect of condition: $F_{1,18}=0.13$, $P=0.73$; frequency X condition interaction: $F_{2,18}=1$, $P=0.39$). **j**, Synchrony after correct decisions did not differ between the RR vs. RS ($n=7$ mice; two-way ANOVA; main effect of condition: $F_{1,18}=0.16$, $P=0.70$; frequency X condition interaction: $F_{2,18}=2.55$, $P=0.11$). **k**, The plot shows the average gamma synchrony on correct vs. incorrect trials, during the first 2 ('early') or next 3 ('late') trials of a rule shift (RS) or rule reversal (RR). In order to average together values from different mice (n = 7), each synchrony value was computed relative to the average gamma synchrony measured during the first 5 RS and RR trials from the same mouse. We performed ANOVA on the gamma synchrony from each of the first 5 trials during a rule shift (RS) or rule reversal (RR), including the following factors and interaction terms: mouse ($F_{6,59}=1.72$, $P=0.13$), type of rule change (RS vs. RR) ($F_{1,59}=3.74$, $P=0.06$), correct vs. incorrect trial outcome ($F_{1,59}=2.64$, $P=0.11$), an interaction of correct-incorrect X RS-RR ($F_{1,59}=11.12$, $^{**}P=0.0015$), and an interaction of correct-incorrect X RS-RR X early vs. late trials (that is first 2 vs. next 3 trials) ($F_{1,59}=4.28$, $^{*}P=0.043$). **l**, Following errors, synchrony during the intertrial interval (ITI) was specifically higher in the 30-50 Hz band during the RS than during the IA ($n=7$ mice; two-way ANOVA; condition X frequency interaction: $F_{4,36}=3.217$, $^{*}P=0.023$; 30-50 Hz: post hoc $t_{(6)}=3.55$, $^{*}P=0.036$) or RR (two-way ANOVA; 30-50 Hz: post hoc $t_{(6)}=3.97$, $^{*}P=0.022$). **m**, Mouse behavior scored during the initial association error ITI for the first 5 IA dual-site TEMPO trials ($n=10$ error ITIs of 8 mice). **n**, Mouse behavior scored during the rule shift error ITI for the first 5 RS dual-site TEMPO trials ($n=17$ error ITIs of 8 mice). There is no difference in seconds of movement between IA and RS (two-tailed, paired *t*-test; $t_{(6)}=0.52$, $P=0.62$) nor in seconds of not moving between IA and RS (two-tailed, paired *t*-test; $t_{(6)}=0.56$, $P=0.59$). Two-way ANOVA followed by Bonferroni post hoc comparisons were used in panels **b**–**c** and **e**–**j**, **l**. Comparisons were not significant unless otherwise noted.

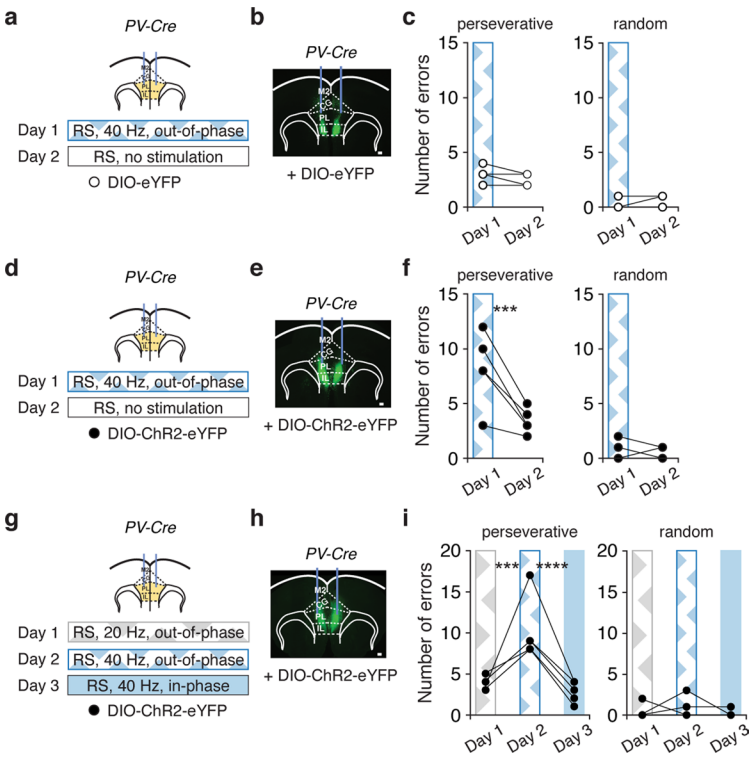

Extended Data Fig. 5 | Types of errors during rule shifts (RS) in the presence of various forms of optogenetic stimulation in PV-Cre mice. a, **d**, *PV-Cre* Ai14 mice had bilateral AAV-DIO-eYFP or AAV-DIO-ChR2 injections and fiber-optic implants in mPFC. Experimental design: Day 1: out-of-phase 40 Hz stimulation during the rule shift (RS); Day 2: no stimulation. **b**, **e**, Representative images showing mPFC expression of eYFP (**b**) or ChR2-eYFP (**e**) (scale bar, 100 μm). **c**, **f**, Optogenetic stimulation increases perseverative errors in ChR2-expressing mice ($n = 5$) compared to eYFP-expressing ($n = 5$ mice) controls (two-way ANOVA; main effect of day: $F_{1,8} = 20.8$, $^{**}P = 0.0018$; main effect of virus: $F_{1,8} = 8.96$, $^{*}P = 0.017$; day X virus interaction: $F_{1,8} = 14.89$, $^{**}P = 0.0048$). There is no change in random errors (two-way ANOVA; main effect of day: $F_{1,8} = 0$, $P > 0.99$; main effect of virus: $F_{1,8} = 0$, $P > 0.99$; day X virus interaction: $F_{1,8} = 0.89$, $P = 0.37$). **c**, Light delivery does not affect the number of perseverative or random errors in eYFP-expressing controls (perseverative: post hoc $t_{(8)} = 0.50$, $P > 0.99$; random: post hoc $t_{(8)} = 0.67$, $P > 0.99$). **f**, Optogenetic stimulation of PV interneurons on Day 1 increased the number of perseverative errors compared to no stimulation on Day 2 (post hoc $t_{(8)} = 5.95$, $^{***}P = 0.0007$), but does not affect random errors (post hoc $t_{(8)} = 0.67$, $P > 0.99$). **g**, *PV-Cre* mice had bilateral AAV-DIO-ChR2-eYFP injections and fiber-optic implants in mPFC. Experimental design: Day 1: out-of-phase 20 Hz stimulation; Day 2: out-of-phase 40 Hz stimulation; Day 3: in-phase 40 Hz stimulation. **h**, Representative image showing mPFC ChR2 expression (scale bar, 100 μm). **i**, Out-of-phase 40 Hz stimulation (Day 2) increases perseverative errors but does not affect random errors, relative to out-of-phase 20 Hz stimulation (Day 1) or in-phase 40 Hz stimulation (Day 3) ($n = 5$ mice; two-way ANOVA; main effect of day: $F_{2,16} = 13.5$, $^{***}P = 0.0004$; Day 1 vs. Day 2 perseverative: $^{***}P = 0.0002$, Day 2 vs. Day 3 perseverative: $^{****}P = 0.00003$, Day 1 vs. Day 3 perseverative: $P > 0.99$; Day 1 vs. Day 2 random: $P > 0.99$, Day 2 vs. Day 3 random: $P > 0.99$, Day 1 vs. Day 3 random: $P > 0.99$). Two-way ANOVA followed by Bonferroni post hoc comparisons were used.

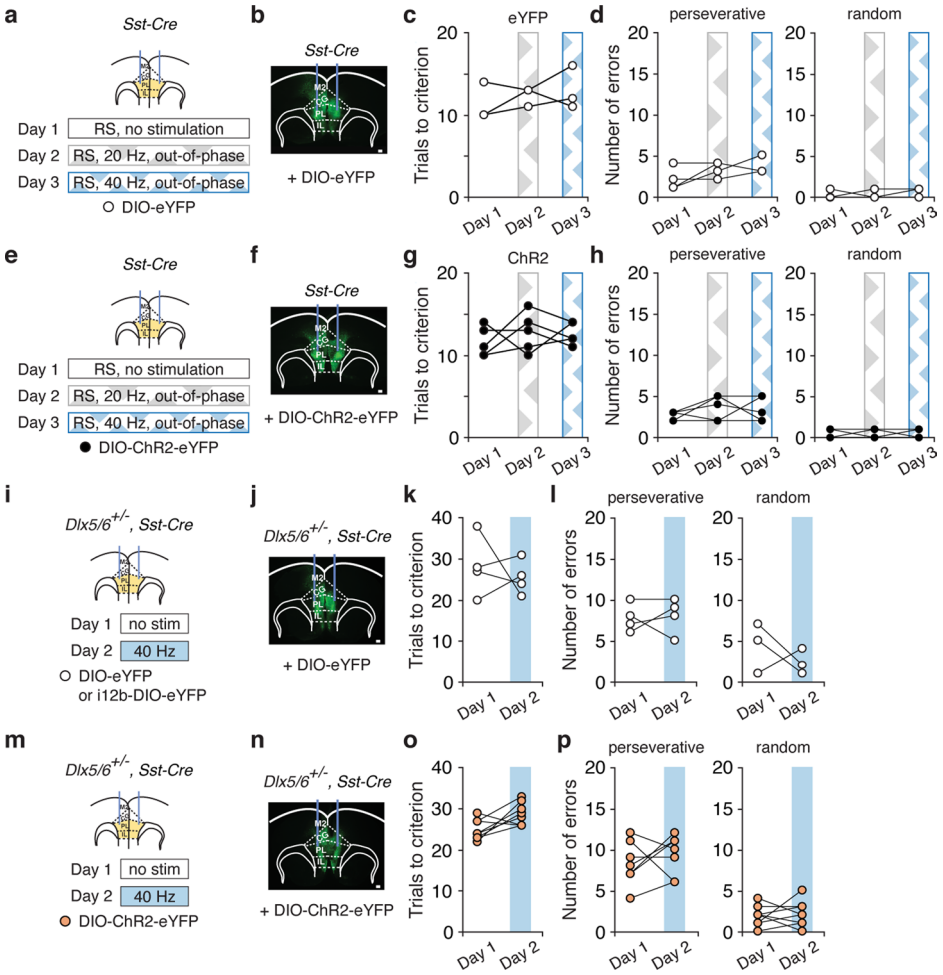

Extended Data Fig. 6 | Behavior and types of errors during rule shifts (RS) in the presence of various forms of optogenetic stimulation in *Dlx5/6*$^{+/-}$, *Sst-Cre* and *Sst-Cre* mice. a, **e**, *Sst-Cre* mice had bilateral injections of AAV-DIO-eYFP (**a**, 'Sst-eYFP') or AAV-DIO-ChR2-eYFP (**e**, 'Sst-ChR2') along with fiber-optic implants in mPFC. Experimental design: Day 1: no light stimulation; Day 2: out-of-phase 20 Hz stimulation; Day 3: out-of-phase 40 Hz stimulation. **b**, Representative image showing mPFC ChR2 expression (scale bar, 100 μm). **c**, **g**, Light delivery did not affect performance in either Sst-eYFP (**c**; $n=4$ mice) or Sst-ChR2 (**g**; $n=5$) mice (two-way ANOVA; main effect of day: $F_{2,14}=2.53$, $P=0.12$; main effect of virus: $F_{1,7}=0.01$, $P=0.92$; day X virus interaction: $F_{2,14}=0.59$, $P=0.57$). **d**, Sst-eYFP mice showed no change in perseverative or random errors from Day 1 to Day 2 to Day 3 ($n=4$ mice; two-way ANOVA; day X type of error interaction: $F_{2,9}=1.18$, $P=0.35$). **h**, Sst-ChR2 mice showed no change in perseverative or random errors from Day 1 to Day 2 to Day 3 ($n=5$ mice; two-way ANOVA; day X type of error interaction: $F_{2,16}=0.81$, $P=0.46$). **i**,**m**, *Dlx5/6*$^{+/-}$, *Sst-Cre* mice had bilateral control virus (AAV-DIO-eYFP or AAV-i12b-DIO-eYFP) or AAV-DIO-ChR2-eYFP (m) injections and fiber-optic implants in mPFC. Experimental design: Day 1: no stimulation; Day 2: 40 Hz stimulation. **j**,**n**, Representative eYFP (**j**) and ChR2-eYFP (**n**) expression in the mPFC of *Dlx5/6*$^{+/-}$, *Sst-Cre* mice (scale bar, 100 μm). **k**,**o**, Light delivery did not affect performance in Sst-eYFP-expressing (**k**; $n=4$ mice) or Sst-ChR2-expressing (**o**; $n=8$) mutant mice (two-way ANOVA; main effect of day: $F_{1,10}=0.08$, $P=0.79$; main effect of virus: $F_{1,10}=0.002$, $P=0.96$; day X virus interaction: $F_{1,10}=2.69$, $P=0.13$). **l**, Sst-eYFP expressing mutants showed no change in perseverative or random errors from Day 1 to Day 2 ($n=4$ mice; two-way ANOVA; day X type of error interaction: $F_{1,6}=0.16$, $P=0.70$). **p**, Sst-ChR2 expressing mutants showed no change in perseverative or random errors from Day 1 to Day 2 ($n=8$ mice; two-way ANOVA; day X type of error interaction: $F_{1,14}=0.64$, $P=0.44$). Two-way ANOVA followed by Bonferroni post hoc comparisons were used. Comparisons were not significant unless otherwise noted.

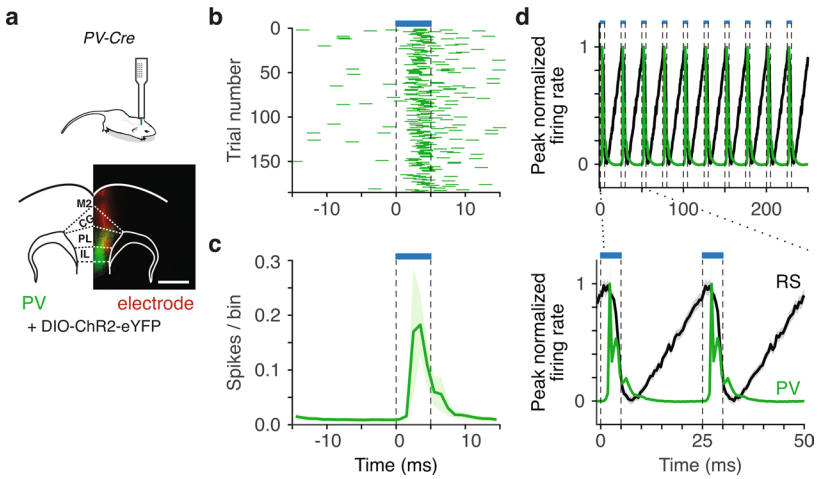

Extended Data Fig. 7 | Single unit recordings from PV interneurons and regular spiking neurons in the mPFC of awake, head-fixed mice. a, Schematic of opto-silicon probe recording PFC in awake head-fixed mice (top panel). Histology of the recording electrode (bottom panel, scale = 1 mm). **b**, Example raster plot of a putative PV cell responding to ChR2 activation. Stimulation at 1 Hz (5 ms illumination, 0.25 mW). The blue line represents the duration of ChR2 stimulation (5 ms). **c**, Average peristimulus time histogram (PSTH) of PV cell responses during 40 Hz ChR2 stimulation ($n = 8$ PV cells, time bin = 1 ms). The blue line indicates the period of ChR2 stimulation (5 ms flash) at 40 Hz. PV cells fired 0.49 ± 10 spikes per 40 Hz cycle at a latency of 1.82 ± 0.34 ms following the onset of each light flash. **d**, Baseline subtracted and peak normalized activity of all putative PV cells (green line; $n = 8$ cells, 3 mice) and all the regular-spiking (RS) cells (black line; $n = 237$ cells, 4 mice). Mean firing rate of RS cells was 4.9 vs. 2.1 spikes/sec at the peak vs. trough of each cycle, respectively. The blue line indicates the period of ChR2 stimulation (5 ms flash) at 40 Hz. Data are shown as means (**c**, **d**) and shading (**c**, **d**) denote s.e.m.

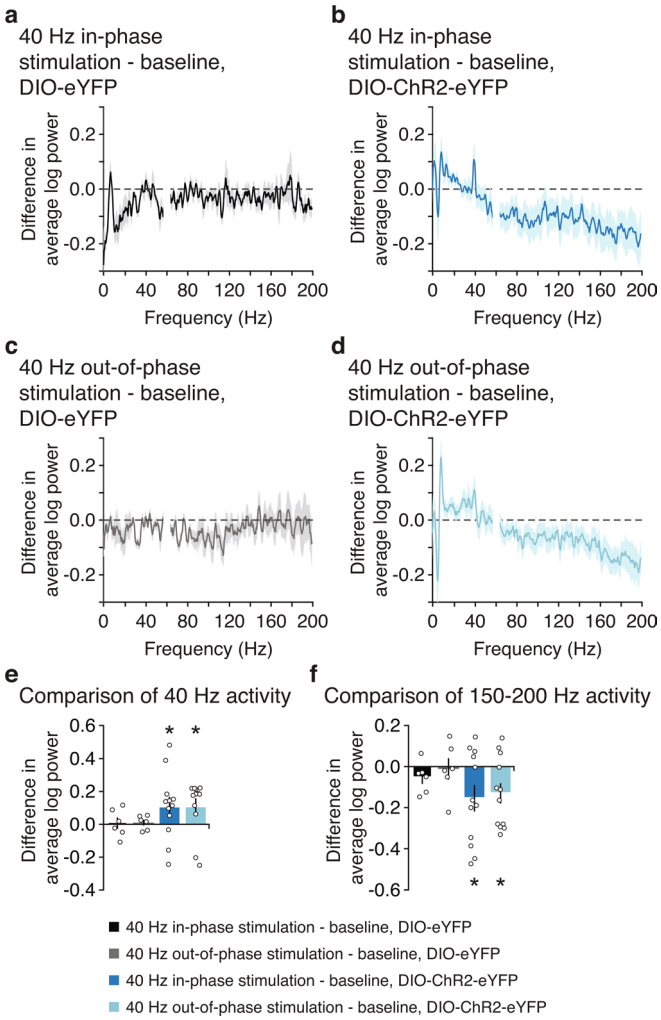

Extended Data Fig. 8 | Changes in the power spectra of prefrontal LFPs elicited by in- vs. out-of-phase stimulation of PV interneurons. a–d, Difference between the power spectra for LFPs recorded during light stimulation vs. at baseline for control mice (*PV-Cre* mice injected with AAV-DIO-eYFP, $n=6$ recordings from 3 mice) receiving (**a**) in- or (**c**) out-of-phase stimulation, or for *PV-Cre* mice ($n=12$ recordings from 6 mice) injected with AAV-DIO-ChR2-eYFP receiving (**b**) in- or (**d**) out-of-phase stimulation. Positive (negative) values correspond to higher power during periods of stimulation (at baseline). **e**, Quantification of average change in 40 Hz power in various conditions (relative to baseline). The change was significantly different from 0 for PV-ChR2 in-phase condition ($n=12$ recordings from 6 mice; two-tailed, paired *t*-test; $t_{(11)}=2.24$, $^*P=0.047$) and for PV-ChR2 out-of-phase condition ($n=12$ recordings from 6 mice; two-tailed, paired *t*-test; $t_{(11)}=2.34$, $^*P=0.039$). **f**, Quantification of average change in 150-200 Hz power in various conditions (relative to baseline). The change was significantly different from 0 for PV-ChR2 in-phase condition ($n=12$ recordings from 6 mice; two-tailed, paired *t*-test; $t_{(11)}=2.40$, $^*P=0.036$) and for PV-ChR2 out-of-phase condition ($n=12$ recordings from 6 mice; two-tailed, paired *t*-test; $t_{(11)}=2.65$, $^*P=0.023$). Two-tailed, paired *t*-tests were used. Data are shown as means; shading (**a–d**) and error bars (**e**,**f**) denote s.e.m.

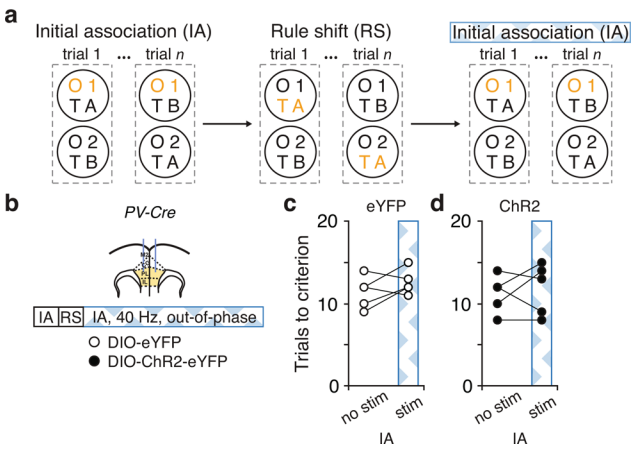

Extended Data Fig. 9 | Out-of-phase 40 Hz stimulation does not disrupt the ability of PV-Cre mice to revert to an initial association. a, Schematic for task: The mouse learns an initial association (IA), then a rule shift (RS). After the mouse learns the RS, the task reverts to the original rule, that is, the rule learned during the IA with out-of-phase 40 Hz stimulation. **b**, *PV-Cre* mice had bilateral AAV-DIO-eYFP ('PV-eYFP') or AAV-DIO-ChR2-eYFP ('PV-ChR2') injections and fiber-optic implants in mPFC. Experimental design: no stimulation during learning of the IA or RS. Then, when the rule reverts to the IA, out-of-phase 40 Hz stimulation is delivered. **c**, In PV-eYFP mice ($n = 5$), there was no difference in the number of trials needed to reach the criterion during initial learning of the IA (when no light was delivered) vs. when reverting to the IA after learning the RS (when light stimulation was delivered; two-tailed, paired *t*-test; $t_{(4)} = 1.31$, $P = 0.261$). **d**, In PV-ChR2 mice ($n = 5$), there was no difference in the number of trials needed to reach the criterion during initial learning of the IA (when no light was delivered) vs. when reverting to the IA after learning the RS (when light stimulation was delivered; two-tailed, paired *t*-test; $t_{(4)} = 0.466$, $P = 0.666$). Two-tailed, paired *t*-tests were used. Comparisons were not significant unless otherwise noted.

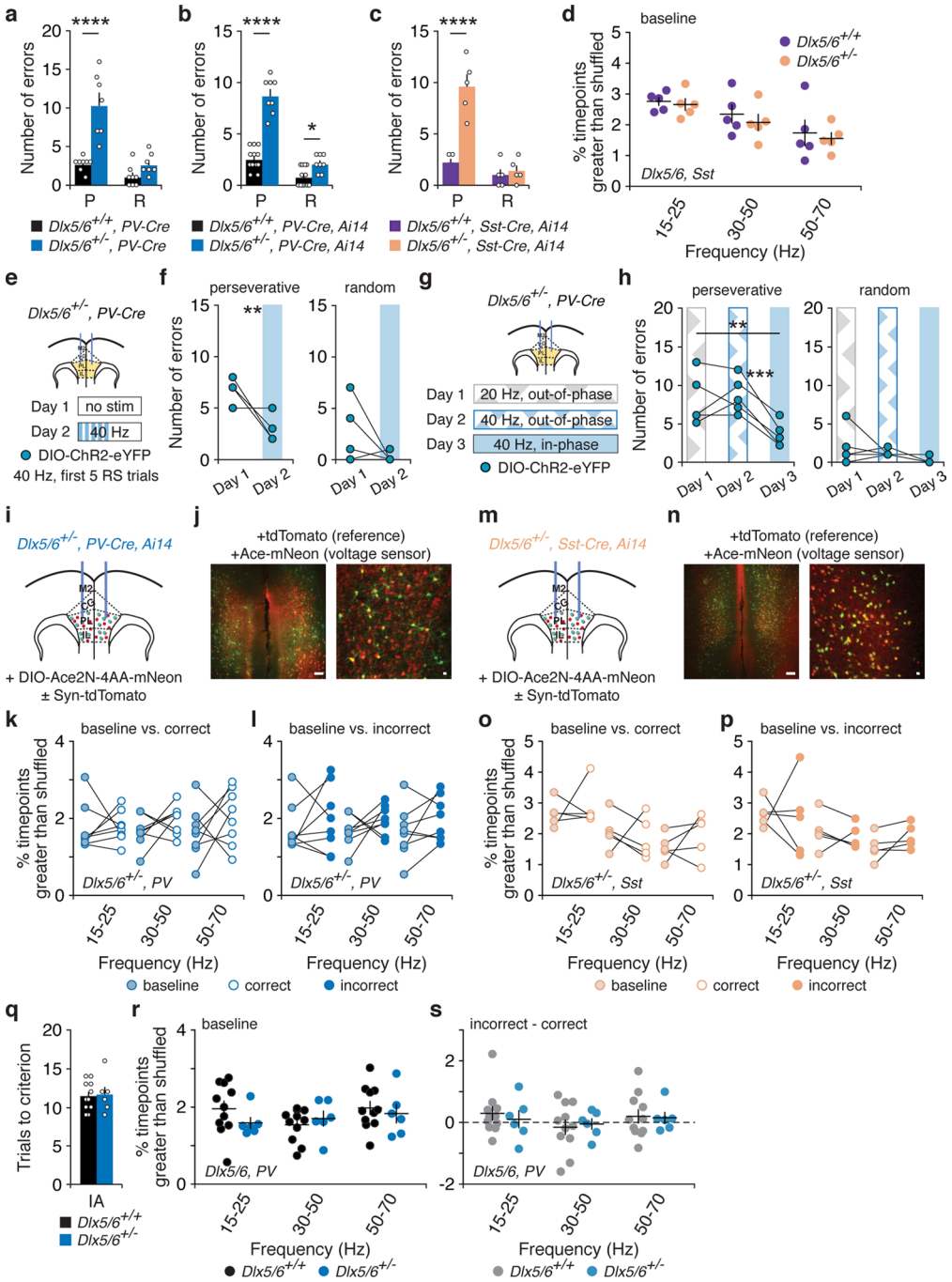

Extended Data Fig. 10 | See next page for caption.

Extended Data Fig. 10 | Behavior and cross-hemispheric synchrony between prefrontal PV or Sst interneurons during rule shifts, baseline periods, or learning of initial associations in *Dlx5/6*$^{+/-}$ mice and wild-types. a, Rule-shift (RS) performance for photometry experiments in *Dlx5/6*$^{+/-}$, *PV-Cre* and *Dlx5/6*$^{+/+}$, *PV-Cre* mice. Compared to wild-type littermates ($n=8$), mutant mice ($n=7$) make more perseverative errors (two-way ANOVA; main effect of genotype: $F_{1,13}=43.6$, $^{****}P=0.00002$; main effect of error type: $F_{1,13}=24.7$, $^{***}P=0.0003$; error type X genotype interaction: $F_{1,13}=10.5$, $^{**}P=0.006$; post hoc $t_{(26)}=6.55$, $^{****}P=0.000001$), but similar numbers of random errors (post hoc $t_{(26)}=1.36$, $P=0.37$). **b**, Rule-shift performance for mice used in dual-site TEMPO experiments. Compared to wild-type mice ($n=12$), mutant mice ($n=8$) make more perseverative errors (two-way ANOVA; main effect of genotype: $F_{1,18}=89.4$, $^{****}P=0.00000002$; main effect of error type: $F_{1,13}=137.3$, $^{****}P=0.0000000007$; type of error X genotype interaction: $F_{1,18}=46.5$, $^{****}P=0.000002$; post hoc $t_{(36)}=11.6$, $^{****}P=0.0000000000002$), and random errors (post hoc $t_{(36)}=2.43$, $^{*}P=0.04$). **c**, Compared to wild-type mice, *Dlx5/6*$^{+/-}$, *Sst-Cre* Ai14 mice make more perseverative errors ($n=5$ mice in each cohort; two-way ANOVA; main effect of genotype: $F_{1,8}=42.3$, $^{***}P=0.0002$; main effect of error type: $F_{1,8}=30.7$, $^{***}P=0.0005$; error type X genotype interaction: $F_{1,8}=17.0$, $^{**}P=0.003$; post hoc $t_{(16)}=7.12$, $^{****}P=0.000005$), but numbers of random errors are comparable (post hoc $t_{(16)}=0.38$, $P>0.99$). **d**, Synchrony was not different between *Dlx5/6*$^{+/+}$, *Sst-Cre* Ai14 and *Dlx5/6*$^{+/-}$, *Sst-Cre* Ai14 mice during the baseline period ($n=5$ mice in each cohort; two-way ANOVA; main effect of genotype: $F_{1,8}=0.77$, $P=0.41$; frequency X genotype interaction: $F_{2,16}=0.05$, $P=0.95$). **e**, *Dlx5/6*$^{+/-}$, *PV-Cre* mice had bilateral AAV-DIO-ChR2-eYFP injections and fiber-optic implants in mPFC. Experimental design: Day 1: no stimulation; Day 2: in-phase 40 Hz stimulation during the first 5 RS trials. **f**, In-phase 40 Hz stimulation on Day 2 reduces perseverative errors relative to no stimulation on Day 1 ($n=6$ mice; two-way ANOVA; main effect of day: $F_{1,10}=18.32$, $^{**}P=0.0016$; main effect of error type: $F_{1,10}=49.9$, $^{****}P=0.000034$; post hoc $t_{(10)}=3.98$, $^{**}P=0.005$); there was no change in random errors (post hoc $t_{(10)}=2.07$, $P=0.13$). **g**, *Dlx5/6*$^{+/-}$, *PV-Cre* mice had bilateral AAV-DIO-ChR2-eYFP injections and fiber-optic implants in mPFC. Experimental design: Day 1: out-of-phase 20 Hz stimulation; Day 2: out-of-phase 40 Hz stimulation; Day 3: in-phase 40 Hz stimulation. **h**, Perseverative errors are reduced by in phase 40 Hz stimulation on Day 3, compared to either out-of-phase 20 Hz stimulation on Day 1 or out-of-phase 40 Hz stimulation on Day 2 ($n=5$ mice; two-way ANOVA; main effect of day: $F_{2,16}=11.6$, $^{***}P=0.0008$; main effect of error type: $F_{1,8}=31.5$, $^{***}P=0.0005$; Day 1 vs. Day 2 perseverative: $P>0.99$, Day 2 vs. Day 3 perseverative: $^{***}P=0.0005$, Day 1 vs. Day 3 perseverative: $^{**}P=0.0016$). There are no changes in random errors across days (post hoc Day 1 vs. Day 2: $P>0.99$, Day 2 vs. Day 3: $P>0.99$, Day 1 vs. Day 3: $P=0.33$). **i**, *Dlx5/6*$^{+/-}$, *PV-Cre* Ai14 mice had bilateral AAV-DIO-Ace2N-4AA-mNeon ± AAV-Syn-tdTomato injections and fiber-optic implants in mPFC. **j**, Representative images of tdTomato (red) and Ace-mNeon (green) fluorescence within PV interneurons in a coronal section of mPFC (left), alongside a high power image (right). Scale bars: 100 μm and 25 μm, respectively. **k**, In mutants, PV interneuron synchrony was not different after correct decisions vs. during the baseline period ($n=8$ mice; two-way ANOVA; main effect of condition: $F_{1,21}=1.89$, $P=0.18$; frequency X condition interaction: $F_{2,21}=0.35$, $P=0.71$). **l**, PV interneuron synchrony was not different after incorrect decisions vs. during the baseline period ($n=8$ mice; two-way ANOVA; main effect of condition: $F_{1,21}=3.31$, $P=0.083$; frequency X condition interaction: $F_{2,21}=0.04$, $P=0.96$). **m**, *Dlx5/6*$^{+/-}$, *Sst-Cre* Ai14 mice had bilateral AAV-DIO-Ace2N-4AA-mNeon ± AAV-Syn-tdTomato injections and fiber-optic implants in mPFC. **n**, Representative images of tdTomato (red) and Ace-mNeon (green) fluorescence in Sst interneurons within a coronal section of mPFC (left) from a *Dlx5/6*$^{+/-}$, *Sst-Cre* Ai14 mouse, alongside a high power image (right). Scale bars: 100 μm and 25 μm, respectively. **o**, In mutants, Sst interneuron synchrony was not different after correct decisions vs. during the baseline period ($n=5$ mice; two-way ANOVA; main effect of frequency: $F_{2,12}=9.88$, $^{**}P=0.003$; frequency X condition interaction: $F_{2,12}=0.58$, $P=0.58$). **p**, Sst interneuron synchrony was not different after incorrect decisions vs. during the baseline period ($n=5$ mice; two-way ANOVA; main effect of frequency: $F_{2,12}=4.95$, $^{*}P=0.027$; frequency X condition interaction: $F_{2,12}=0.44$, $P=0.66$). **q**, Learning of an initial association (IA) was similar in mutants ($n=6$) and their wild-type ($n=11$) littermates (two-tailed, unpaired *t*-test; $n=11$; $t_{(15)}=0.202$, $P=0.842$). **r**, There was no difference in cross-hemispheric PV interneuron synchronization between mutant ($n=6$ mice) and wild-type ($n=11$ mice) littermates at baseline (two-way ANOVA; main effect of genotype: $F_{1,15}=0.45$, $P=0.51$; genotype X frequency interaction $F_{2,30}=1.11$, $P=0.34$). **s**, During learning of an initial association, changes in PV interneuron synchrony following errors (relative to synchrony after correct decisions) are similar in mutants ($n=6$ mice) and their wild-type ($n=11$ mice) littermates (two-way ANOVA; main effect of genotype: $F_{1,15}=0.07$, $P=0.80$; genotype X frequency interaction: $F_{2,30}=0.16$, $P=0.86$). Data are shown as means (**a**–**c**); error bars (**a**–**c**) denote s.e.m. Two-way ANOVA followed by Bonferroni post hoc comparisons were used. Comparisons were not significant unless otherwise noted.

nature research

Corresponding author(s): Vikaas Sohal

Last updated by author(s): Apr 6, 2020

Reporting Summary

Nature Research wishes to improve the reproducibility of the work that we publish. This form provides structure for consistency and transparency in reporting. For further information on Nature Research policies, see Authors & Referees and the Editorial Policy Checklist.

Statistics

For all statistical analyses, confirm that the following items are present in the figure legend, table legend, main text, or Methods section.

n/a	Confirmed	
☐	☒	The exact sample size (*n*) for each experimental group/condition, given as a discrete number and unit of measurement
☐	☒	A statement on whether measurements were taken from distinct samples or whether the same sample was measured repeatedly
☐	☒	The statistical test(s) used AND whether they are one- or two-sided *Only common tests should be described solely by name; describe more complex techniques in the Methods section.*
☐	☒	A description of all covariates tested
☐	☒	A description of any assumptions or corrections, such as tests of normality and adjustment for multiple comparisons
☐	☒	A full description of the statistical parameters including central tendency (e.g. means) or other basic estimates (e.g. regression coefficient) AND variation (e.g. standard deviation) or associated estimates of uncertainty (e.g. confidence intervals)
☐	☒	For null hypothesis testing, the test statistic (e.g. *F*, *t*, *r*) with confidence intervals, effect sizes, degrees of freedom and *P* value noted *Give P values as exact values whenever suitable.*
☒	☐	For Bayesian analysis, information on the choice of priors and Markov chain Monte Carlo settings
☒	☐	For hierarchical and complex designs, identification of the appropriate level for tests and full reporting of outcomes
☒	☐	Estimates of effect sizes (e.g. Cohen's *d*, Pearson's *r*), indicating how they were calculated

Our web collection on statistics for biologists contains articles on many of the points above.

Software and code

Policy information about availability of computer code

Data collection	Synapse 84 (Tucker-Davis Technologies), Sirenia Acquisition 1.7.5 (Pinnacle Technology, Inc.)
Data analysis	Statistical analyses were performed in Matlab (Mathworks) and Prism 7 (GraphPad). OpenScope (Tucker-Davis Technologies) was used for behavioral scoring. Image processing was performed using ImageJ. Adobe Illustrator was used for assembling figures.

For manuscripts utilizing custom algorithms or software that are central to the research but not yet described in published literature, software must be made available to editors/reviewers. We strongly encourage code deposition in a community repository (e.g. GitHub). See the Nature Research guidelines for submitting code & software for further information.

Data

Policy information about availability of data

All manuscripts must include a data availability statement. This statement should provide the following information, where applicable:

- Accession codes, unique identifiers, or web links for publicly available datasets
- A list of figures that have associated raw data
- A description of any restrictions on data availability

The source data for all figures is included. The raw data supporting the findings of this study are available from the corresponding author upon reasonable request.

Field-specific reporting

Please select the one below that is the best fit for your research. If you are not sure, read the appropriate sections before making your selection.

☒ Life sciences ☐ Behavioural & social sciences ☐ Ecological, evolutionary & environmental sciences

Life sciences study design

All studies must disclose on these points even when the disclosure is negative.

Sample size	No statistical methods were used to predetermine sample size, but sample size choice was based on previous studies (Cho et al., 2015) and are consistent with those generally employed in the field.
Data exclusions	For analysis of single unit recording, we excluded units with refractory 30 period violations greater than 1%. Mice that did not make both correct and incorrect decisions in the first 5 trials of a task could not be used for analyses which compared activity on correct vs. incorrect decisions. No other data were excluded. In all behavioral experiments (optogenetics, fiber photometry, LFP, dual-site voltage-sensor (TEMPO) photometry), we verified that viral expression and/or electrode/fiber tip placement was in the target structure.
Replication	All key findings were replicated in new cohorts, and all attempts at replication were successful.
Randomization	Animals were randomly assigned numbers and tested blind for the experimental condition.
Blinding	All behavioral experiments were performed, scored, and analyzed blind to the genotype, virus injected, etc.

Reporting for specific materials, systems and methods

We require information from authors about some types of materials, experimental systems and methods used in many studies. Here, indicate whether each material, system or method listed is relevant to your study. If you are not sure if a list item applies to your research, read the appropriate section before selecting a response.

Materials & experimental systems

n/a	Involved in the study
☒	☐ Antibodies
☒	☐ Eukaryotic cell lines
☒	☐ Palaeontology
☐	☒ Animals and other organisms
☒	☐ Human research participants
☒	☐ Clinical data

Methods

n/a	Involved in the study
☒	☐ ChIP-seq
☒	☐ Flow cytometry
☒	☐ MRI-based neuroimaging

Animals and other organisms

Policy information about studies involving animals; ARRIVE guidelines recommended for reporting animal research

Laboratory animals	Male and female mice of the following strains were used, at 10-20 weeks of age: PV-Cre, Sst-Cre, Ai14 (all from The Jackson Laboratory) and Dlx5/6 mice. The Dlx5/6 mice (provided by J.L.R. Rubenstein) were backcrossed to C57Bl/6 mice (The Jackson Laboratory) for at least 6 generations before being crossed to C57Bl/6 PV-Cre, Sst-Cre, and Ai14 lines.
Wild animals	The study did not involve wild animals.
Field-collected samples	The study did not involve samples collected from the field.
Ethics oversight	All animal care, procedures, and experiments were conducted in accordance with the NIH guidelines and approved by the Administrative Panels on Laboratory Animal Care at the University of California, San Francisco.

Note that full information on the approval of the study protocol must also be provided in the manuscript.